

RESEARCH ARTICLE SUMMARY

EPIGENETIC MEDICINE

Brainwide silencing of prion protein by AAV-mediated delivery of an engineered compact epigenetic editor

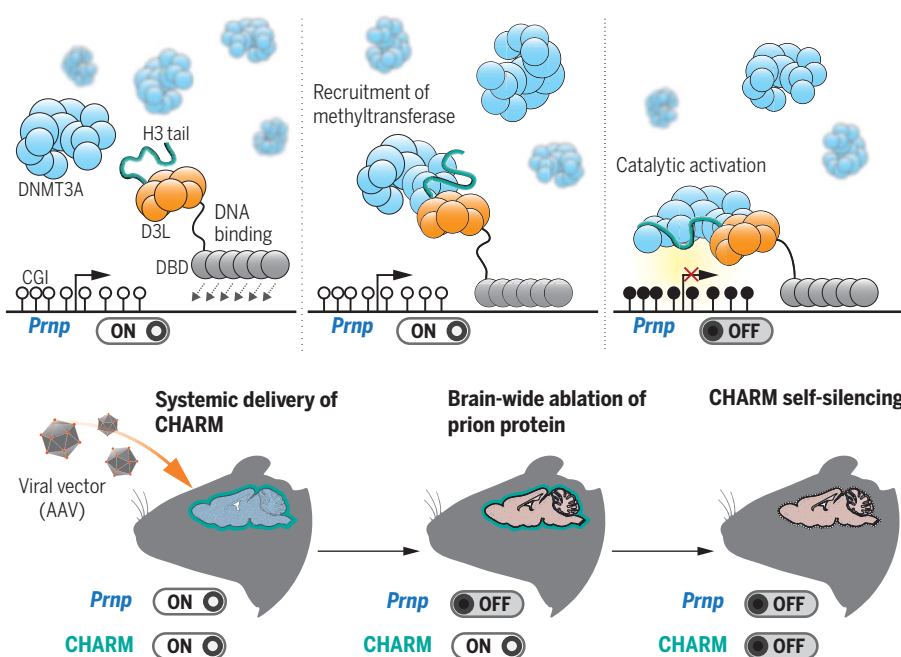
Edwin N. Neumann[†], Tessa M. Bertozzi[†], Elaine Wu, Fiona Serack, John W. Harvey, Pamela P. Brauer, Catherine P. Pirtle, Alissa Coffey, Michael Howard, Nikita Kamath, Kenney Lenz, Kenia Guzman, Michael H. Raymond, Ahmad S. Khalil, Benjamin E. Deverman, Eric Vallabh Minikel, Sonia M. Vallabh*, Jonathan S. Weissman*

INTRODUCTION: Prion diseases are fatal neurodegenerative disorders caused by misfolding of the prion protein in the brain. Cases can manifest spontaneously, be inherited genetically, or be acquired through transmission (e.g., mad cow disease). Although there are currently no effective treatments, reducing prion protein levels in the brain has been shown to halt disease progression in animal models with minimal adverse effects. In addition, prion protein is nonessential in mammals, indicating that lowering its expression in the brain is a viable therapeutic strategy.

RATIONALE: Genetic medicines hold great promise but are often difficult to translate to the clinic. Current CRISPR-based DNA-editing technologies are complex large molecules that are challenging to deliver and have been associated with unintended editing outcomes. We therefore favored an epigenetic editing approach to permanently turn off prion protein expression in the brain without altering the underlying DNA sequence or leading to continued expression of an altered mRNA and protein. This strategy uses DNA methylation to achieve long-term transcriptional silencing. However, current epigenetic editors are cytotoxic in some circumstances and are too large to fit in an adeno-associated virus (AAV) vector, the preferred delivery vehicle to the central nervous system.

RESULTS: To address these challenges, we engineered a compact, enzyme-free epigenetic editor termed CHARM (Coupled Histone tail for Autoinhibition Release of Methyltransferase). Through a direct fusion with the histone H3 tail and a noncatalytic Dnmt3l domain, CHARM is able to recruit and activate DNA methyltransferases endogenously expressed in the cell to methylate the target gene. CHARM can act independently of KRAB transcriptional repression domains and is compatible with multiple DNA-binding modalities, including CRISPR-Cas, transcription activator-like effectors, and zinc finger proteins. The small size of zinc finger proteins enables up to three DNA targeting elements to be accommodated in a single AAV with additional room for regulatory elements to confer cell-type specificity. When coupled to a prion protein-targeting zinc finger domain and delivered to the mouse brain through AAV, CHARM methylates the prion gene promoter and achieves up to 80% brainwide reduction in neuronal prion protein, far exceeding the minimal reduction required for therapeutic benefit. Furthermore, we developed self-silencing CHARMS that autonomously deactivate themselves after silencing their target. This approach temporally limits CHARM expression to circumvent potential antigenicity and off-target activity resulting from chronic expression in nondividing neurons.

CONCLUSION: This study represents the first demonstration of AAV-mediated delivery of an epigenetic editor that can programmably methylate DNA in the brain for durable, potent silencing of a target gene. CHARM avoids overexpression of potentially cytotoxic catalytic domains by harnessing the endogenous DNA methylation machinery. Its compact size enables modular self-silencing strategies, facilitates multiplexed targeting, and enhances compatibility with other delivery modalities, such as lipid nanoparticles. This work could enable an effective treatment for patients with prion disease as well as other neurodegenerative diseases involving the accumulation of toxic protein aggregates. More generally, CHARM represents the next generation of safe and easily deliverable epigenetic editors for therapeutic intervention and biological discovery. ■



CHARM is an epigenetic editor for targeted DNA methylation and gene silencing. (Top) CHARM consists of a DNA binding domain (DBD) fused to the Dnmt3l domain (D3L) and histone H3 tail. CHARM is targeted to the prion protein (*Prnp*) promoter, D3L recruits the endogenous methyltransferase DNMT3A, and the H3 tail activates DNMT3A to silence *Prnp* through methylation of the cytosine-guanine dinucleotide (CpG) island (CGI). (Bottom) AAV-delivered CHARM silences *Prnp* throughout the mouse brain. Self-silencing of CHARM temporally limits its expression.

The list of author affiliations is available in the full article online.

*Corresponding author. Email: weissman@wi.mit.edu (J.S.W.); svallabh@broadinstitute.org (S.M.V.)

†These authors contributed equally to this work.

Cite this article as E. N. Neumann et al., *Science* **384**, eado7082 (2024). DOI: 10.1126/science.ado7082

S READ THE FULL ARTICLE AT
<https://doi.org/10.1126/science.ado7082>

RESEARCH ARTICLE

EPIGENETIC MEDICINE

Brainwide silencing of prion protein by AAV-mediated delivery of an engineered compact epigenetic editor

Edwin N. Neumann^{1,2†}, Tessa M. Bertozzi^{1,3†}, Elaine Wu¹, Fiona Serack⁴, John W. Harvey⁴, Pamela P. Brauer⁴, Catherine P. Pirtle⁴, Alissa Coffey⁴, Michael Howard⁵, Nikita Kamath⁴, Kenney Lenz⁵, Kenia Guzman⁵, Michael H. Raymond^{6,7}, Ahmad S. Khalil^{6,7,8}, Benjamin E. Deverman⁴, Eric Vallabh Minikel^{4,9}, Sonia M. Vallabh^{4,9*}, Jonathan S. Weissman^{1,3,10,11*}

Prion disease is caused by misfolding of the prion protein (PrP) into pathogenic self-propagating conformations, leading to rapid-onset dementia and death. However, elimination of endogenous PrP halts prion disease progression. In this study, we describe Coupled Histone tail for Autoinhibition Release of Methyltransferase (CHARM), a compact, enzyme-free epigenetic editor capable of silencing transcription through programmable DNA methylation. Using a histone H3 tail-Dnmt3l fusion, CHARM recruits and activates endogenous DNA methyltransferases, thereby reducing transgene size and cytotoxicity. When delivered to the mouse brain by systemic injection of adeno-associated virus (AAV), *Prnp*-targeted CHARM ablates PrP expression across the brain. Furthermore, we have temporally limited editor expression by implementing a kinetically tuned self-silencing approach. CHARM potentially represents a broadly applicable strategy to suppress pathogenic proteins, including those implicated in other neurodegenerative diseases.

Prión disease is caused by misfolding of the endogenous prion protein, PrP, initiating a chain reaction of templated misfolding to form toxic aggregates that cause neuronal death (1). PrP misfolding can occur spontaneously, the likelihood of which is increased by certain genetic mutations or as the result of infection with misfolded prion seeds (1, 2). All subtypes of prion disease—including Creutzfeldt-Jakob disease (CJD), fatal familial insomnia (FFI), Kuru, and Gerstmann-Sträussler-Scheinker (GSS) disease in humans, as well as scrapie, chronic wasting disease, and bovine spongiform encephalopathy (or mad cow disease) in animals—are caused by PrP (1). Despite the rarity of prion disease (3),

our deep molecular understanding of its etiology provides a path toward potential treatment and prevention (2). Mice lacking *Prnp*, the gene encoding PrP, are resistant to prion infection (4), and depletion of PrP expressed in neurons after infection is sufficient to prevent prion disease progression and reverse symptoms in mice (5). Treatment of mice with antisense oligonucleotides (ASOs) targeting the *Prnp* transcript decreases expression of PrP and extends the survival of mice previously infected with misfolded PrP (6); however, the limited efficacy of ASOs and the requirement for chronic intrathecal dosing highlight the need for a more potent therapy. Both engineered and naturally occurring *PRNP* knockouts are well-tolerated in a variety of mammals (7–11). The only known knockout phenotype relates to disruption of a myelin maintenance signaling pathway (12) in which homozygous knockouts exhibit mild peripheral neuropathy (13, 14). These data indicate that strategies aimed at reducing PrP expression in neurons represent a viable therapeutic approach even after the onset of symptoms. Lessons learned in the development of this therapeutic approach may be applied to other neurodegenerative diseases, as there is now accumulating evidence that Parkinson's, Alzheimer's, Huntington's, and other dementias involve protein aggregation as a central component of pathogenesis that can be targeted for therapeutic benefit (15, 16). Indeed, monoclonal antibodies targeting amyloid- β plaques in early Alzheimer's disease patients show a modest delay in cognitive decline (17).

Epi genetic silencing represents an attractive approach for eliminating expression of pathogenic proteins such as PrP without the need to mutate the underlying DNA sequence (18–24). Permanent silencing can be achieved through targeted DNA methylation by the recruitment of the constitutively active catalytic domain (D3A) of the de novo DNA methyltransferase enzyme DNMT3A (25–27) along with the C-terminal domain (D3L) of its cofactor DNMT3L (28–30). DNA methylation at cytosine-guanine dinucleotide (CpG) sites, producing 5-methyl-CpGs (5mCpGs), is mitotically inherited and contributes to transcriptional silencing directly by blocking transcription factor binding and indirectly by recruiting methyl-CpG-binding factors that induce heterochromatin (31). These domains, with the addition of a repressive KRAB domain, were fused to a nuclease-deficient *Streptococcus pyogenes* Cas9 (dSpCas9), yielding a CRISPR-based editor for programmable, heritable gene silencing termed CRISPRoff (32). CRISPRoff has the benefit of a wide and effective targeting window at gene promoters as a result of CpG methylation spreading, and its effect is generally stable through cell division and differentiation. This stands in contrast to CRISPRi (dCas9-KRAB), which enables robust but transient gene repression (18). Additionally, genome-wide screening indicated that the large majority of genes can be silenced with CRISPRoff (32). Prion disease is an excellent candidate for this approach because simply decreasing PrP expression will have a therapeutic effect (2) and because the human *PRNP* promoter contains a large annotated CpG island to serve as a substrate for DNA methylation. However, the complexity of the CRISPRoff system leads to challenges for delivery and toxicity as a therapeutic and necessitates the development of a more compact, potent, and safe epigenetic silencer.

Results

The prion gene is a viable target for durable epigenetic silencing

We first assessed the suitability of the mouse and human *PRNP* gene to epigenetic silencing with targeted DNA methylation using CRISPRoff. We transduced human embryonic kidney 293T (HEK293T) cells with a single-guide RNA (sgRNA) targeting the transcription start site (TSS) of the *PRNP* gene. CRISPRoff and CRISPRi (18) were introduced by transient transfection, and PrP expression was assessed by flow cytometry with fluorescent anti-PrP antibodies (Fig. 1A). With a transient pulse of CRISPRoff effector, *PRNP* remains durably silenced for at least 50 days. As expected, the repressive effect of CRISPRi was reversed rapidly upon loss of effector expression (Fig. 1B). Target-enriched nanopore sequencing of native DNA confirmed extensive multi-kb DNA methylation across the CpG island of the *PRNP* promoter region with

¹Whitehead Institute for Biomedical Research, Cambridge, MA 02142, USA. ²Department of Biological Engineering, Massachusetts Institute of Technology, Cambridge, MA 02139, USA. ³Howard Hughes Medical Institute, Massachusetts Institute of Technology, Cambridge, MA 02142, USA. ⁴Stanley Center for Psychiatric Research, Broad Institute of MIT and Harvard, Cambridge, MA 02142, USA.

⁵Comparative Medicine, Broad Institute of MIT and Harvard, Cambridge, MA 02142, USA. ⁶Biological Design Center, Boston University, Boston, MA 02215, USA. ⁷Department of Biomedical Engineering, Boston University, Boston, MA 02215, USA. ⁸Wyss Institute for Biologically Inspired Engineering, Harvard University, Boston, MA 02115, USA.

⁹McCance Center for Brain Health and Department of Neurology, Massachusetts General Hospital, Boston, MA 02114, USA. ¹⁰Department of Biology, Massachusetts Institute of Technology, Cambridge, MA 02139, USA.

¹¹David H. Koch Institute for Integrative Cancer Research, Massachusetts Institute of Technology, Cambridge, MA 02142, USA.
*Corresponding author. Email: weissman@wi.mit.edu (J.S.W.); svallabh@broadinstitute.org (S.M.V.)
†These authors contributed equally to this work.

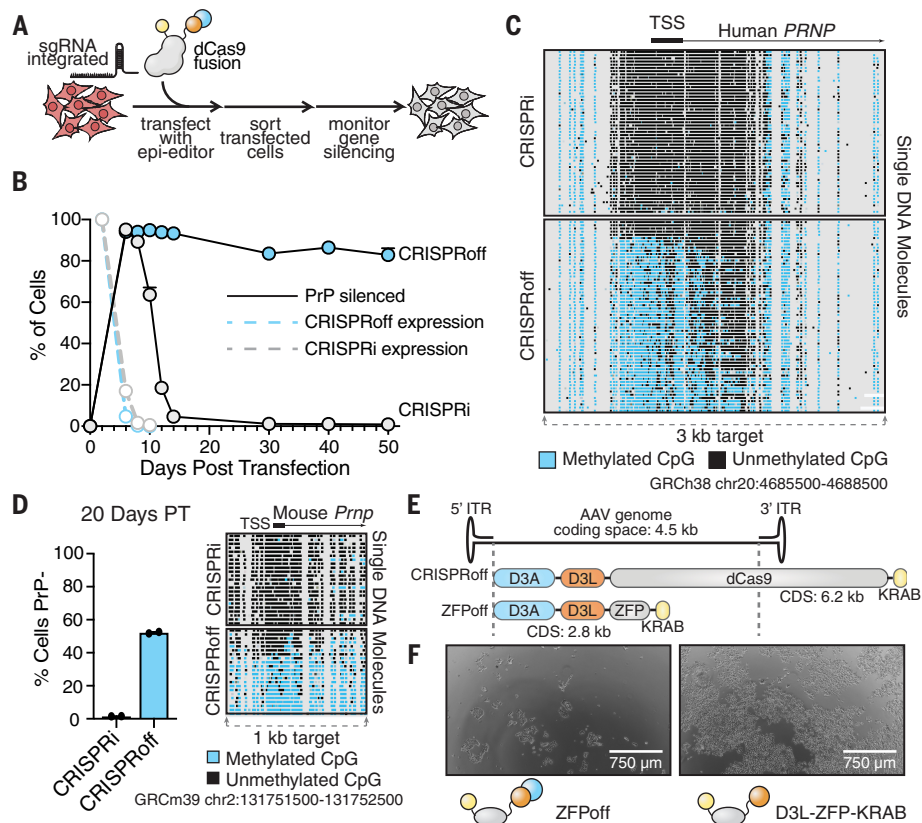


Fig. 1. *PRNP* is a viable target for epigenetic silencing, but existing technologies are not suitable for therapeutic use. (A) A HEK293T cell line was made by integrating a lentiviral vector containing mU6-sgRNA targeting the *PRNP* TSS. Transfected cells were sorted by FACS (TagBFP) 2 days after transfection and monitored for *PRNP* silencing by Alexa Fluor 647 anti-PrP staining and flow cytometry. (B) PrP and effector expression time course of HEK293T cells transiently transfected with plasmids encoding CRISPRi and CRISPRoff effectors. Data are mean \pm SEM of $n = 2$ replicates. (C) DNA methylation assessment by targeted nanopore long-read sequencing of native genomic DNA extracted from HEK293T cells 50 days after transfection. (D) Mouse N2a cells cotransfected with plasmids encoding CRISPRi and CRISPRoff and three sgRNAs targeting the TSS of *Prnp* were assessed for PrP expression and DNA methylation. (E) Schematic depicting AAV genome packaging constraints with CRISPRoff and ZFPoff to scale. (F) HEK293T cells were transiently transfected with ZFPoff and D3L-ZFP-KRAB and imaged after 6 days.

the CRISPRoff treatment but not with CRISPRi (Fig. 1C). Similarly, targeting of CRISPRoff to mouse *Prnp* in Neuro-2a (N2a) cells led to silencing and DNA methylation (Fig. 1D and fig. S1), confirming that mice would be a viable model for in vivo prion repression experiments with our epigenetic editor (epi-editor; see below).

Existing epigenome editors are too large or too toxic for therapeutic use

In its present form, CRISPRoff is poorly suited to be a therapeutic for prion disease. The preferred vehicle for transgene delivery to the central nervous system (CNS) is the adeno-associated virus (AAV), which can be efficiently packaged with cargo around 4.7 kb in length, including inverted terminal repeats (33). The D3A-D3L-dCas9-KRAB fusion comprising CRISPRoff is ~6.2 kb long, far exceeding the packaging capacity of an AAV vector (Fig.

1E). Most of this space is occupied by the 4.1-kb coding sequence of dSpCas9. Moreover, given that AAV genomes form concatenated episomes that chronically express the transgene, the bacterial enzyme Cas9 is likely to become antigenic over time (34, 35); a large proportion of the human population already has an immune memory of it (36). To overcome these obstacles, dCas9 can be replaced with a different DNA binding modality.

Zinc finger proteins (ZFPs) are ubiquitous DNA binding proteins in eukaryotes (37) whose modular nature has enabled programming for specific genome targeting (38–42). ZFPs offer some advantages as a therapeutically relevant DNA targeting module; their compact size, roughly an order of magnitude smaller than that of SpCas9, makes them suitable for delivery through AAV (Fig. 1E), and they are also less immunogenic owing to their lack of bacterial epitopes (43). Previous work has motivated

our interest in using ZFPs in our effector constructs for targeted and heritable gene silencing for the reason that engineered ZFPs fused to chromatin-modifying domains have successfully modulated gene transcription in vivo as long as they are continuously expressed (44–47).

The next challenge to overcome is cytotoxicity. The full-length de novo DNMT3 methyltransferases are regulated by an autoinhibitory mechanism (48), which CRISPRoff bypasses by only using the catalytically active methyltransferase domain D3A (32). The D3A domain on its own can have detrimental effects when overexpressed in target cells; indeed, a ZFPoff construct transiently overexpressed in HEK293T cells exhibited substantial cytotoxicity, whereas cells transfected by the same ZFP fusion without the D3A catalytic domain recovered quickly (Fig. 1F and see below). Attempts to instead recruit full-length DNMT3A for DNA methylation have previously been described (49). Accordingly, we tried using a single green fluorescent protein (GFP) nanobody (50) to bind enhanced GFP (EGFP)-tagged DNMT3A, a strategy that has been efficacious for the recruitment of other repressive domains (51), but we observed poor activity (fig. S2, A and B).

The dominant de novo methyltransferase in somatic tissues, particularly in the brain, is the isoform DNMT3A1, whereas DNMT3B is virtually nonexistent (52); all subsequent mentions of DNMT3A refer to DNMT3A1. DNMT3A normally exists in an autoinhibited conformation in which its methyltransferase domain is occluded by its ADD domain, and this is only released upon binding of the ADD domain to unmethylated histone H3 lysine 4 (H3K4me0), which is methylated near active promoters, resulting in DNAme inversely correlated with H3K4 methylation (53–55). This mechanism couples DNMT3A activity to its two chromatin-reading domains: the ADD domain, which reads H3K4me0, and the PWWP domain, which reads di- and trimethylated histone H3 lysine 36 (H3K36me2/3) enriched in transcribed gene bodies (48) (fig. S3A). In vitro, purified DNMT3A is stimulated by a 12-amino acid H3K4me0 peptide to methylate a substrate (53, 55, 56). Furthermore, DNMT3A complexes with DNMT3L in a 2:2 stoichiometry through hydrophobic contacts in their C-terminal domains (57). This suggests that DNMT3L, which is catalytically inactive and has an ADD domain of its own (fig. S3B), may help stabilize DNMT3A and could assist the active methyltransferase in seeking an appropriate target for DNAme (58). DNMT3L coimmunoprecipitation experiments indicate that it interacts with both DNMT3A and DNMT3B to coordinate de novo DNAme (59). These interactions are the key to exploiting the endogenous pool of de novo methyltransferases for epigenetic editing strategies, thus removing the need to overexpress toxic quantities of the D3A catalytic domain.

A fusion of the histone H3 tail and Dnmt3l C-terminal domain efficiently mediates heritable gene silencing in cells

Taking advantage of the known interactions between DNMT3A, DNMT3L, and H3K4me0, we developed a strategy for targeted DNA methylation and epigenetic silencing—analogous to but distinct from CRISPRoff—by leveraging the use of the endogenous methyltransferases in cells. Rather than overexpressing the D3A methyltransferase domain as a fusion protein, we instead recruit the full-length enzyme to the target site through interactions with the D3L domain and stimulate its activity using an unmethylated H3 tail fused to the N terminus of the epi-editor. We named this new effector CHARM: Coupled Histone tail for Autoinhibition Release of Methyltransferase (Fig. 2A).

Using the *CLTA* gene tagged with mScarlet as a fluorescent reporter for endogenous gene silencing in HEK293T cells, we systematically compared several epi-editors, including the canonical CRISPRoff and CRISPRi constructs. As expected, CRISPRoff silenced the reporter durably, CRISPRi repressed the reporter transiently, and D3L-dCas9 had a minimal silencing effect. The 12-amino acid H3K4me0 peptide fused to D3L-dCas9 resulted in silencing almost on par with CRISPRoff despite lacking the KRAB domain. To demonstrate that the unmethylated H3K4 residue is critical for endogenous DNMT3A stimulation, we mutated the lysine to alanine (H3A4). This mutant resulted in no silencing improvement over D3L-dCas9 alone (Fig. 2B). The H3 tail fusion was particularly sensitive to linker modifications connecting it to the D3L domain; in the first round of testing, only a 40-amino acid linker could achieve robust silencing (Fig. 2C). We further showed the importance of the autoinhibition release mechanism of the CHARM system by testing full-length DNMT3A direct fusions on our *CLTA* reporter, in which only the truncated D3A catalytic domain achieved the full silencing effect analogous to histone tail-mediated activation (fig. S3C).

To verify that this effect is due to the mechanism of histone tail binding the ADD domain of the methyltransferase rather than simply stabilizing or altering expression of the fusion protein, we performed a transfection-dose titration, comparing D3L with or without the H3 tail. At 18 days after transfection, there was little difference in silencing activity across transfected DNA concentrations, indicating that the epi-editor is unlikely to be dose-limited (fig S4A). Likewise, gating for different levels of expression while sorting the transfected cells did not improve silencing efficacy by day 16 after transfection (fig. S4B). This indicates that activity of the epi-editor is not limited by translation or stability of the fusion protein.

CHARM optimization

We next sought to optimize the CHARM effector by manipulating various parameters of the fusion protein. First, we tested a range of linker lengths centered around the established 40-amino acid length. We also modified the canonical extended recombinant polypeptide (XTEN) linker amino acid sequence to increase the flexibility through the removal of proline residues to generate the “midiflex” and “maxiflex” linker variants following general linker engineering guidelines (60). The 40-amino acid maxiflex linker provided a modest increase in silencing activity, and this epi-editor was denoted CRISPRcharm1 (Fig. 2D). Attempts to boost activity by increasing nuclear localization through the addition of an N-terminal nuclear localization signal (NLS) or by appending two H3 tails in tandem were unsuccessful (fig. S4C), suggesting that having a free N terminus is critical for CHARM function. Furthermore, fusions of either the H3 tail or D3L alone to dCas9 had lower silencing capability than the two together, indicating a synergistic rather than additive effect (fig. S4D).

Another variable to optimize was the D3L domain sequence, which is critical for methyltransferase recruitment and stabilization. Rather than performing random mutagenesis, we restricted our exploration to the extant universe of D3L domains orthologous to the canonical *Mus musculus* D3L, as well as some ancestral sequence reconstructions (ASRs) (61) between the rodent and primate clades (Fig. 2E). Approximately two dozen D3L orthologs and ASRs fused to dCas9 were tested on the *CLTA* reporter, with the most active being the D3L domain of the European wood mouse *Apodemus sylvaticus* (AsD3L) (Fig. 2F). This epi-editor became CRISPRcharm2.

Although the first 12 amino acids of the histone H3 tail were sufficient to stimulate methylation activity, we speculated that a longer portion of the flexible tail region of histone H3.1 could have a higher affinity for the ADD domain of DNMT3A. When recruited to our *CLTA* reporter with a mismatched sgRNA to avoid saturation of the transcriptional silencing signal, a 30-amino acid H3 tail, but not the full H3.1 protein including the globular domain, resulted in a more potent CHARM effector (Fig. 2G); this was designated CRISPRcharm3. Consistent with the proposed mechanism of CHARM, we found that CHARM requires DNMT3A (and not DNMT3B) by knocking out the de novo methyltransferases in our *CLTA* reporter cells, whereas this genetic background did not impact silencing efficacy with exogenously supplied D3A (Fig. 2H and fig. S4E). These optimization efforts led to a CHARM effector exceeding the transcriptional silencing capabilities of CRISPRoff (Fig. 2I) when a KRAB domain was fused to the C terminus of dCas9, as occurs in CRISPRoff (32). Schematics of

each of these CHARM epi-editors can be found in fig. S4F, with the optimized version without the KRAB domain subsequently referred to as CRISPRcharm.

We further observed that the KRAB domain could be incorporated into the flexible linker between the H3 tail and D3L. The two KRAB domain-containing variants were named CRISPRcharm Kv1 and Kv2, respectively, and both can efficiently repress the *CLTA* reporter (fig. S4G). To test the breadth of targeting capabilities of our new CHARM effector, we targeted CRISPRoff, CRISPRcharm, and CRISPRcharm Kv2 to three cell-surface markers using HEK293T cells with preintegrated sgRNAs. Antibody staining and flow cytometry revealed durable repression out to about 3 weeks, on par with CRISPRoff (Fig. 2J), suggesting that CHARMs will be effective on the broad range of genes amenable to DNA methylation-mediated silencing (32).

CHARMs are compatible with different DNA binding domains

After optimizing the CHARM effector using CRISPR-dCas9 recruitment to our endogenous *CLTA* reporter, we next explored the potential of using different DNA binding modalities to reduce transgene size and facilitate packaging into an AAV vector. We replaced dCas9 in CRISPRcharm Kv1 with previously published ZFPs developed by Sangamo Therapeutics and targeting the mouse *Prnp* promoter (ZFPs 81187 and 81201) (62) to generate ZFcharm Kv1. These were transiently transfected into N2a cells and achieved durable (>1 month) PrP silencing (Fig. 3A). Transcription activator-like effectors (TALEs), another mode of programmable DNA binding domain, have also been shown to enable targeted DNA methylation (29). TALEs can be easier to design than ZFPs, so we constructed chimeric TALEs (63) fused to the CHARM effector (denoted TALEcharm) to target the mouse *Prnp* promoter, with some success (Fig. 3B).

The relatively small size of ZFcharms and TALEcharms enables flexible single-vector AAV packaging strategies with the potential for multiplexed targeting. Inspired by recent work for AAV delivery of base editors (64), we leveraged the split *Nostoc punctiforme* (Npu) intein strategy for trans-splicing (65) of polypeptides. We constructed ZFcharms with the CHARM effector (with N-terminal Npu intein) separated from the ZFP DNA binding domain (with C-terminal Npu intein) by 2A ribosome skipping sequences, thus generating two distinct polypeptide chains from the same mRNA transcript. These polypeptides are spliced together to form the complete ZFcharm Kv2 molecule and are as effective at silencing *PRNP* as direct fusions (fig. S5A). Building on this idea, we propose multiple AAV cargo designs that fall within the 5-kb AAV genome limit and enable multiplexed targeting by distinct DNA

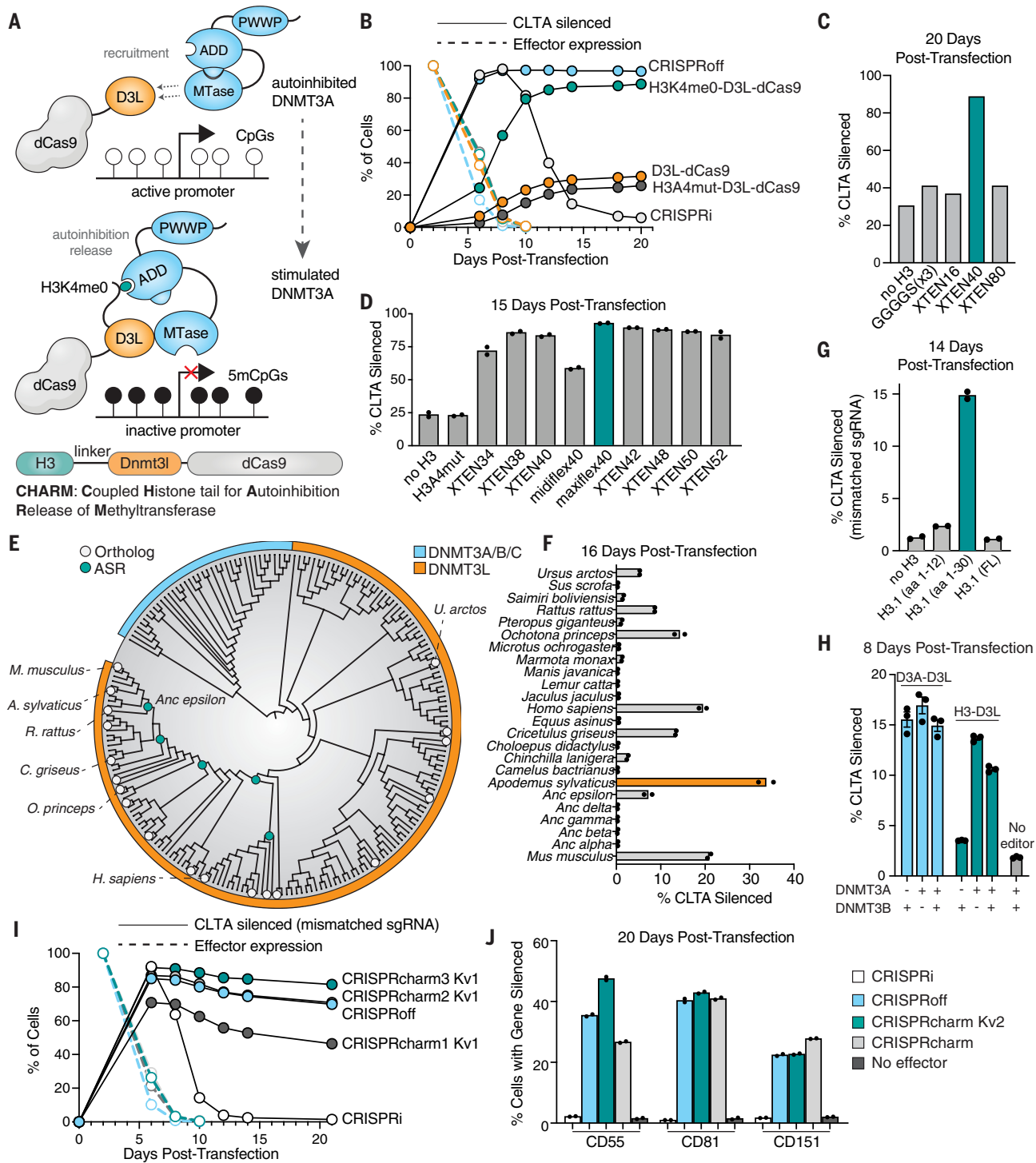
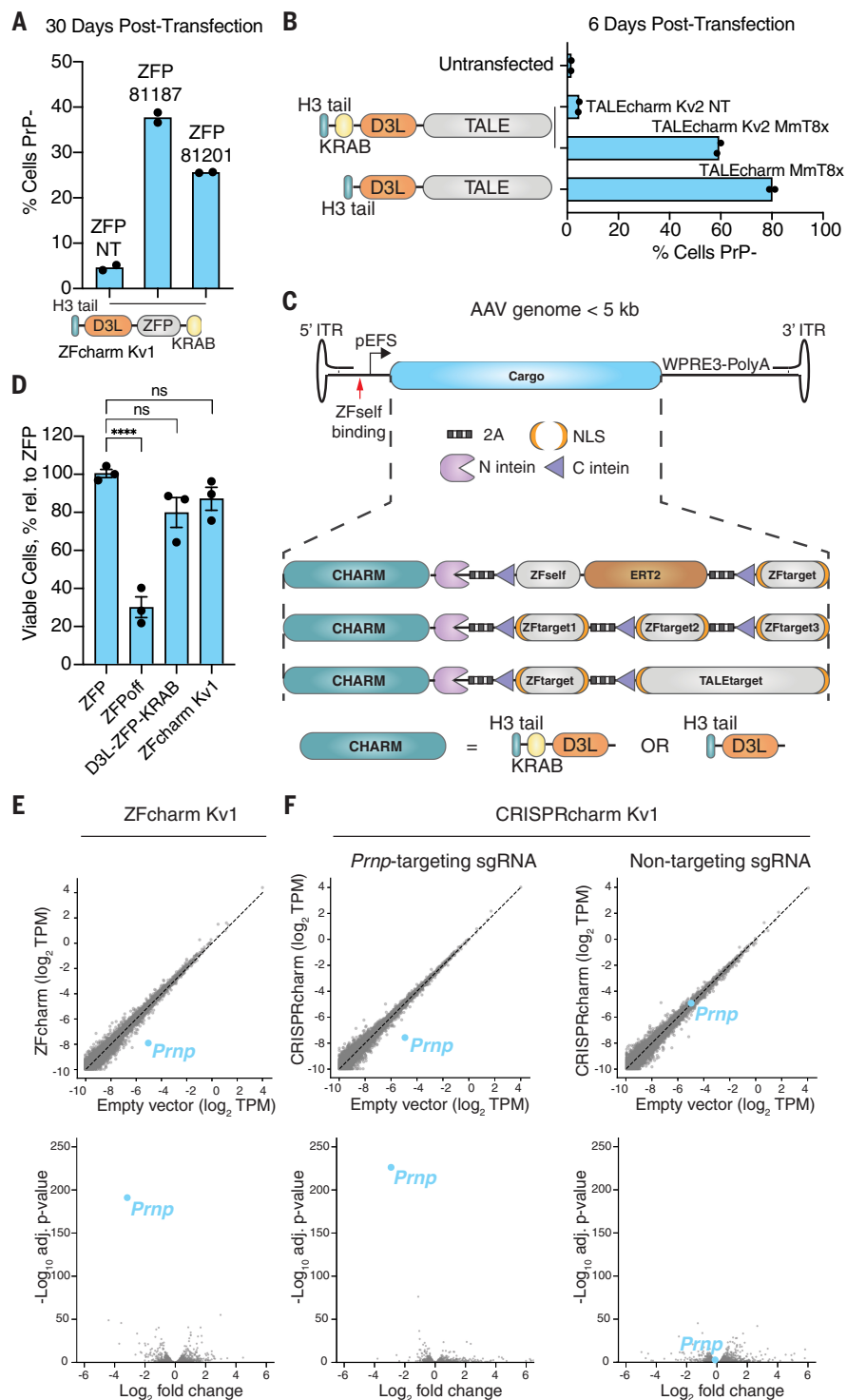


Fig. 2. A histone H3 tail fused to the Dnmt3l C-terminal domain acts as a potent mediator of DNA methylation and transcriptional silencing. (A) Cartoon depiction of endogenous DNMT3A recruitment and activation by the CHARM system. (B) Time course of effector (TagBFP) and mScarlet-CLTA reporter expression after transient transfection with effector-containing plasmids. Data are mean \pm SEM of $n = 2$ replicates. (C) First pass histone H3 tail fusion test on the mScarlet-CLTA reporter performed using different linkers to D3L. (D) Refinement of linker sequence between H3 tail and D3L. (E) Phylogenetic tree of DNMT3L orthologs and ancestral reconstruction nodes. Orthologs with measured silencing activity >5% by 14 days are labeled. (F) Repression of mScarlet-CLTA reporter 2 weeks after transfection with different DNMT3L ortholog C-terminal domains fused to dCas9. (G) Transient transfection and repression of mScarlet-CLTA reporter with different length histone isoform H3.1 domains (FL; full length). A mismatched sgRNA against CLTA TSS is used to improve dynamic range. (H) Transient transfection of sgRNA and effector fused to dCas9 targeting the CLTA reporter in a methyltransferase knockout background. Data are mean \pm SEM of $n = 3$ replicates. (I) Time course of effector expression and mScarlet-CLTA silencing comparing CRISPRoff and CRISPRcharm against the series of optimized CHARM constructs. Data are mean \pm SEM of $n = 2$ replicates. (J) Comparison of CRISPRi, CRISPRoff, and the optimized CRISPRcharm effectors in silencing cell-surface markers. Vectors encoding mU6-sgRNAs were transduced through lentivirus, and effector plasmids were transiently transfected.

different DNMT3L ortholog C-terminal domains fused to dCas9. (G) Transient transfection and repression of mScarlet-CLTA reporter with different length histone isoform H3.1 domains (FL; full length). A mismatched sgRNA against CLTA TSS is used to improve dynamic range. (H) Transient transfection of sgRNA and effector fused to dCas9 targeting the CLTA reporter in a methyltransferase knockout background. Data are mean \pm SEM of $n = 3$ replicates. (I) Time course of effector expression and mScarlet-CLTA silencing comparing CRISPRoff and CRISPRcharm against the series of optimized CHARM constructs. Data are mean \pm SEM of $n = 2$ replicates. (J) Comparison of CRISPRi, CRISPRoff, and the optimized CRISPRcharm effectors in silencing cell-surface markers. Vectors encoding mU6-sgRNAs were transduced through lentivirus, and effector plasmids were transiently transfected.

Fig. 3. CHARM is flexible and specific. (A) Mouse N2a cells were transiently transfected with plasmids encoding ZFcharm Kv1 constructed with the mouse *Prnp*-targeting ZFP 81187, ZFP 81201, or a nontargeting ZFP and stained with Alexa Fluor 647 anti-PrP. (B) Mouse N2a cells were transiently transfected with TALEcharms and TALEcharm Kv2 composed of engineered TALE proteins targeting the mouse *Prnp* TSS or a nontargeting TALE, then measured using Alexa Fluor 647 anti-PrP. (C) Schematic of AAV packaging using space-saving techniques such as split inteins (65) or a self-silencing approach including the tamoxifen-inducible engineered estrogen receptor ERT2 (66). WPRE3 is a structured 3' element for mRNA stability (67). (D) HEK293T cells were transiently transfected with plasmids encoding ZFP81187 alone or the fusions ZFOff, D3L-ZFP-KRAB, and ZFcharm Kv1 and then counted by flow cytometry after cell viability staining with LIVE/DEAD near-infrared dye (Invitrogen). Data are mean \pm SEM of $n = 3$ replicates. Statistical analyses are one-way analyses of variance (ANOVAs) followed by Tukey's multiple comparisons test. **** $P < 0.0001$; ns, not significant. (E and F) ZFcharm Kv1 (E) and CRISPRcharms Kv1 (F) were introduced into N2a cells by lentiviral transduction and assessed for *Prnp* knockdown and specificity by RNA sequencing 4 weeks later. CRISPRcharms Kv1 was evaluated in N2a cells expressing sgRNA targeting the mouse *Prnp* TSS or a nontargeting sgRNA. Volcano plots (upper) and \log_2 fold changes (lower) were generated from DESeq2.



binding domains while only encoding a single CHARM effector in the transgene. The compact size even allows more sophisticated approaches for small-molecule control of gene silencing, such as through inducible nuclear localization of an engineered estrogen receptor when bound to tamoxifen, as well as enabling inclusion of the WPRE3 RNA-stabilizing element (66, 67) (Fig. 3C).

For the remaining observations, we focused on the use of ZFPs for DNA target engagement. However, we observed efficient targeting and gene silencing with both *S. pyogenes* CRISPR-Cas9 and TALE modalities. It is thus highly likely that CHARM effectors will be broadly compatible with other DNA binding domains; indeed, we demonstrated efficient silencing of our CLTA reporter using a nuclease-deficient version

of the smaller *S. aureus* Cas9 (dSaCas9) more amenable to AAV packaging (68) (fig. S5B).

CHARMs exhibit low toxicity with high specificity

We observed marked cytotoxicity associated with transient overexpression of ZFOff but not with D3L-ZFP-KRAB lacking the catalytic D3A domain (see above). This led us to hypothesize that ZFcharms, which replace D3A with a

short-histone tail peptide and have no catalytic activity on their own, would be better-tolerated in cells. By transiently transfecting HEK293T cells, performing fluorescence-activated cell sorting (FACS) to isolate transfected cells, and then staining and counting cells with a viability dye, we quantified the cytotoxicity of ZFcharm Kv1 expression. ZFOff-transfected cells were significantly less viable 6 days after transfection, whereas ZFcharm Kv1-transfected cells were indistinguishable from cells transfected with ZFP lacking any effector domains (Fig. 3D).

To assess the specificity of ZFcharm Kv1, we performed RNA sequencing 28 days after transduction of N2a cells by lentivirus-containing ZFcharm Kv1 targeting *Prnp* and saw minimal off-target gene repression (Fig. 3E). This is consistent with our analysis of N2a cells transduced with CRISPRcharm Kv1 and sgRNA targeting *Prnp* or with a nontargeting sgRNA (Fig. 3F), suggesting that CHARM expression has minimal bystander effects and that its specificity is largely dictated by the DNA binding domain. Likewise, we quantified the knockdown of *Prnp* transcripts and saw nearly complete repression when compared to nontargeting or effector-null conditions (fig. S6).

AAV-delivered CHARMS lead to brainwide *Prnp* repression and methylation

Having achieved CHARM-mediated heritable *Prnp* silencing in cultured cells, we tested silencing efficacy *in vivo* through AAV delivery to the mouse brain. Constructs with and without the KRAB domain (ZFcharm Kv1 and ZFcharm, respectively) were packaged into AAV-PHP.eB, a capsid engineered for high transduction efficiency throughout the mouse CNS (69). We intravenously administered 1.5×10^{13} viral genomes per kilogram (vg/kg) AAV to adult mice via retro-orbital injections and harvested whole brains 6 weeks later (Fig. 4A). *Prnp* reverse transcription quantitative polymerase chain reaction (RT-qPCR) and PrP enzyme-linked immunosorbent assay (ELISA) on homogenized whole-brain hemispheres revealed a 70 to 90% decrease in *Prnp* transcripts and a 60 to 80% reduction in PrP protein levels, with the protein knockdown possibly muted by ELISA floor effects (70). In addition, ZFcharm constructs lacking the KRAB domain were highly effective, suggesting that DNA methylation alone is sufficient to silence *Prnp* in the brain (Fig. 4B). These levels of knockdown far exceed those previously achieved through ASO delivery shown to be protective against prion disease (6). Doubling the AAV dose led to a mild improvement in *Prnp* repression and reduced interindividual variability (Fig. 4C). No adverse effects were detected at any of the administered doses, but subsequent experiments were conducted at the intermediate dose of 1.5×10^{13} vg/kg, given that the higher dose yielded modest gains. Nanopore sequencing of the 3 kb surrounding the *Prnp*

promoter region showed that both ZFcharm and ZFcharm Kv1 established DNA methylation of CpGs surrounding the TSS (Fig. 4D and fig. S7). These data argue that CHARMS can recruit de novo DNA methyltransferases endogenously expressed in the brain and effectively release enzymatic autoinhibition *in vivo*.

We carried out *in situ* hybridization chain reaction (HCR) RNA-FISH (*fluorescence in situ hybridization*) on coronal brain sections to visualize *Prnp* expression 6 weeks after injection. Robust *Prnp* silencing was evident throughout the section, highlighting the broad CNS biodistribution attained by the AAV-PHP.eB capsid (Fig. 4E). Using HCR probes targeting the pan-neuronal marker *Uchl1*, we evaluated neuronal *Prnp* expression in ZFcharm Kv1-treated and untreated brains. Whereas *Prnp* and *Uchl1* expression was colocalized throughout untreated brains, a decrease in *Prnp* signal was evident in most *Uchl1*⁺ cells within treated brains (Fig. 4F). This effect was quantified at the single-cell level by using QuPath software (71), revealing that ZFcharm Kv1 effectively silenced *Prnp* in the vast majority of neurons, which is consistent with the data from whole-brain hemisphere homogenate (Fig. 4, B and G to I, and fig. S8, A and B). This analysis establishes CHARM as a potent epigenetic silencer in the therapeutically relevant cell type, as *Prnp* depletion in neurons alone is sufficient to prevent prion disease in mice (5, 72, 73). More broadly, it demonstrates that the CHARM technology is functional in postmitotic cells.

CHARMs can be programmed for time-limited expression through self-silencing

AAV-mediated delivery of transgenes in non-dividing cells results in chronic expression from episomal AAV genomes, raising antigenicity and off-target editing concerns. As a result, previous efforts have aimed to restrict AAV expression once the desired therapeutic edits are accomplished (74–76). However, in the case of CRISPR cutting, this is at the cost of increased AAV transgene genomic insertions. Epi-editors are well-suited for a self-silencing approach in that they do not induce DNA damage nor require constitutive expression to maintain target-gene silencing.

To achieve this, we developed self-silencing CHARMS, which silence their own promoter after silencing their target. We installed the ZFP binding motif from the *Prnp* promoter at positions flanking the core EF1α (EFS) promoter driving CHARM expression, allowing the ZF domain to bind both the *Prnp* and EFS promoters (Fig. 5A). Self-silencing kinetics were assessed in N2a cells by measuring ZFcharm Kv1 and *Prnp* expression over time after lentiviral transduction with constructs containing the following binding site configurations: (i) a scrambled sequence as a negative control (scrambled; ZFcharm Kv1-SCR), (ii) one binding

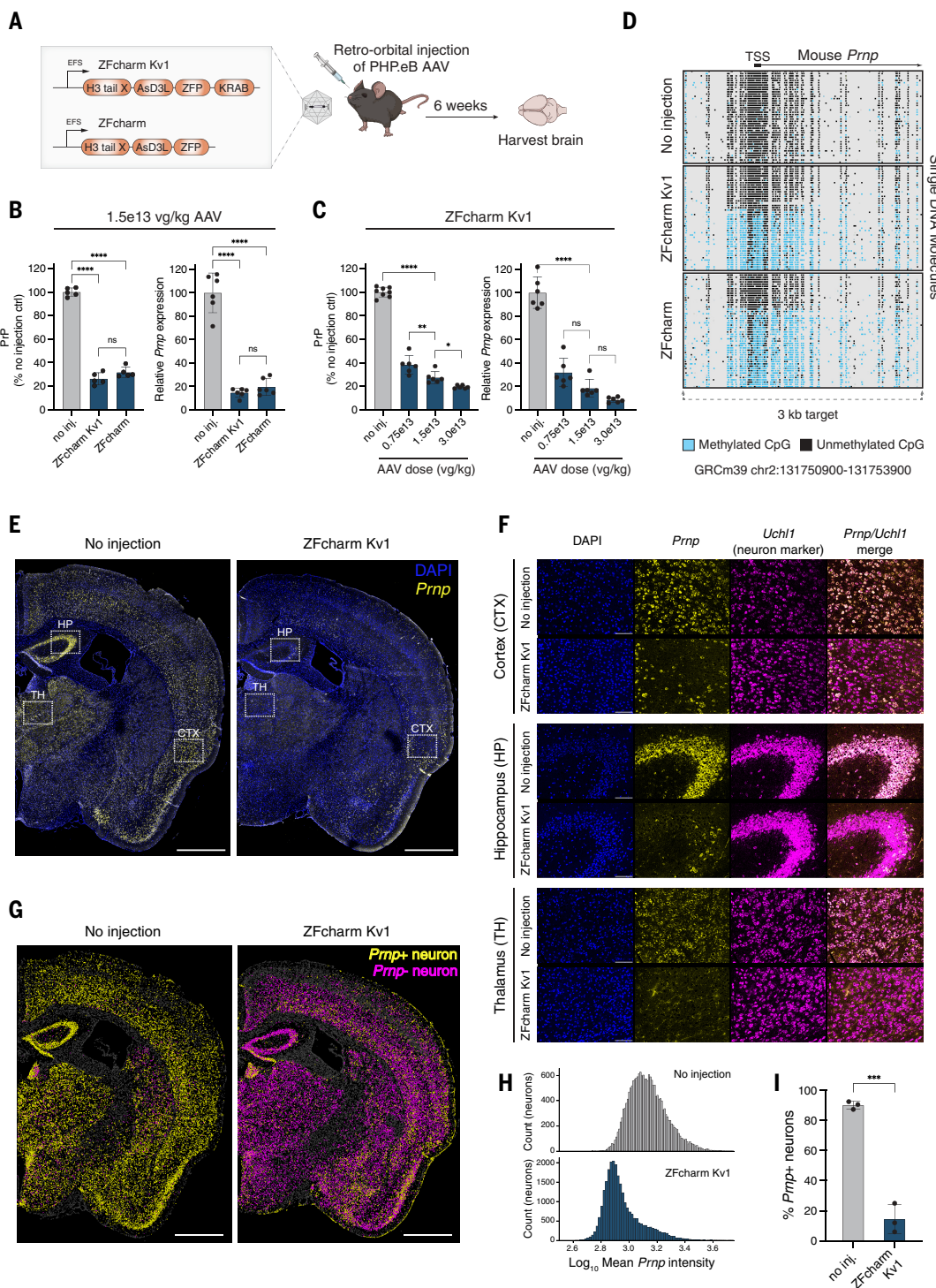
site upstream of the promoter with a mismatch to decrease binding affinity (single mismatch; ZFcharm Kv1-SMM), (iii) one binding site upstream of the promoter (single perfect match; ZFcharm Kv1-SPM), and (iv) two binding sites flanking the promoter (double perfect match; ZFcharm Kv1-DPM) (Fig. 5, A and B).

Flow cytometry quantification after lentiviral transduction showed that all constructs initially induced complete repression of *Prnp* as well as differential rates of self-silencing, with only the SPM and DPM constructs showing self-silencing 6 days after transduction (Fig. 5C). By 60 days after transduction, ZFcharm Kv1 was fully silenced across all conditions, yet *Prnp* was reactivated in a subset of cells transduced with ZFcharm Kv1-DPM. Our interpretation is that the KRAB domain facilitated complete repression of *Prnp* initially but that self-silencing occurred too rapidly to establish lasting repression through DNA methylation (Fig. 5C). These findings are generalizable beyond lentiviral assays because integrating the self-silencing constructs by means of the *piggyBac* transposase system produced consistent results (fig. S9A).

We selected ZFcharm Kv1-SPM for further characterization, as it minimized the length of CHARM expression without compromising heritable silencing. Clonal bisulfite sequencing of the ZFcharm Kv1-SPM promoter in N2a cells revealed an accumulation of DNA methylation 5 days after transduction, particularly between the TATA box and the TSS (Fig. 5D and fig. S9, B and C). By day 25, this region was completely methylated (Fig. 5D and fig. S9, B and C). The promoter with a scrambled binding site also gained methylation over time, but in a slower and more dispersed fashion (Fig. 5D and fig. S9B). We attribute this gain in methylation and eventual loss of ZFcharm Kv1-SCR expression to self-silencing-independent transgene silencing (77).

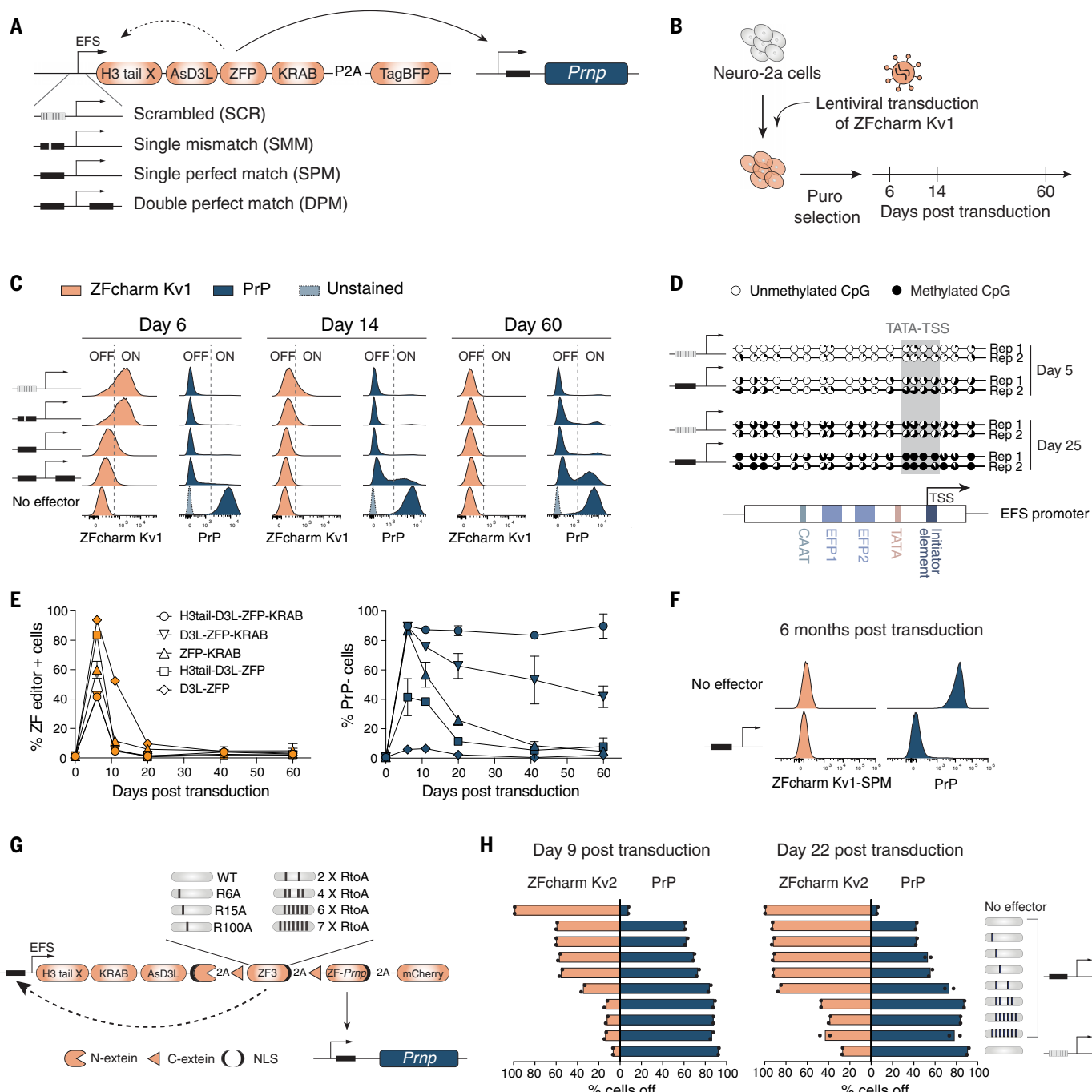
To investigate the essentiality of each ZFcharm component, we compared ZFcharm Kv1-SPM with other ZF-SPM constructs lacking one or more domains. Although all editors became self-silenced, only ZFcharm Kv1-SPM showed stable repression of *Prnp* over time (Fig. 5E and fig. S9D). Notably, *Prnp* remained transcriptionally silent 6 months after ZFcharm Kv1-SPM transduction in N2a cells (Fig. 5F). In contrast to our *in vivo* data, the KRAB domain was required for robust *Prnp* repression in the context of dividing cells in culture (Fig. 4B, Fig. 5E, and fig. S9D). Inclusion of the KRAB domain in CHARM constructs should therefore be determined on a locus-by-locus basis according to efficacy and off-target profiles.

We next engineered a more modular self-silencing ZFcharm Kv2, which eliminates the need to adjust self-silencing kinetics for each new target. To accomplish this, we integrated two ZF domains into our lentiviral construct, with one exclusively responsible for self-silencing

**Fig. 4.** AAV-delivered ZFcharms repress and methylate *Prnp* in vivo.

(A) Schematic of experimental design. ZFcharm Kv1 and ZFcharm were delivered to mice through AAV, and whole brains were harvested 6 weeks later. Unless otherwise noted, the AAV dose was 1.5×10^{13} vg/kg. (B) PrP ELISA and *Prnp* RT-qPCR data generated from brain hemisphere homogenate 6 weeks after injection. Data are mean \pm SD of $n = 5$ to 6 replicates. (C) ZFcharm Kv1 AAV dose-response analysis. Data are mean \pm SD of $n = 6$ to 8 replicates. (D) Quantification of DNA methylation through nanopore sequencing of the *Prnp* promoter. (E and F) Visualization of *Prnp* (yellow) and pan-neuronal marker *Uchl1* (magenta) expression in coronal brain sections through HCR RNA-FISH [DAPI (4',6-diamidino-2-phenylindole) staining in blue]. (E) Representative maximum-intensity projections

of coronal brain hemisphere tile scans. White boxes indicate brain regions shown in (F). Scale bars, 1 mm. (F) Zoomed-in views of the cortex (CTX), hippocampus (HP), and thalamus (TH) regions shown in (E). Scale bars, 100 μ m. (G) Machine learning classification of *Prnp*+ (yellow) and *Prnp*- (magenta) neurons performed with QuPath software (71). *Uchl1*- cells are shown in gray. Cell boundaries represent 4- μ m expansions from DAPI-detected nuclei. Scale bars, 1 mm. (H) Representative histograms of mean *Prnp* intensity in neurons. (I) Bar chart showing % *Prnp*+ neurons in treated and untreated brains according to QuPath classification. Data are mean \pm SD of $n = 3$ replicates. Statistical analyses are one-way ANOVAs followed by Tukey's multiple comparisons test for (B) and (C), and unpaired *t* test for (I). * $P < 0.05$, ** $P < 0.005$, *** $P < 0.0005$, **** $P < 0.0001$; ns, not significant.

**Fig. 5. Transient CHARM expression through self-silencing is sufficient**

for persistent PrP repression. Self-silencing kinetics were quantified by measuring CHARM (orange; TagBFP or mCherry) and PrP (navy; Alexa Fluor 647 anti-PrP) expression over time through flow cytometry after lentiviral transduction of N2a cells. (A) Schematic of self-silencing CHARM constructs. (B) Schematic of experimental design. (C) Representative flow cytometry histograms of ZFcharm Kv1 and PrP expression at days 6, 14, and 60 after transduction. Dashed line indicates separation between expressing (ON) and silenced (OFF) cells. (D) Clonal bisulfite sequencing of EFS promoters driving ZFcharm Kv1-SCR and ZFcharm Kv1-SPM expression 5 and 25 days after transduction of N2a cells. The % 5mCpG (black) across PCR clones is

depicted with pie charts. Sequence elements within the EFS promoter are shown in the schematic under the data. CpGs between the TATA box and TSS are highlighted in gray. (E) 60-day flow cytometry time course monitoring ZF editor and PrP expression across ZF-SPM constructs. Data are mean \pm SD of $n = 2$ replicates. (F) ZFcharm Kv1-SPM and PrP expression 6 months after transduction ($n = 1$). (G) Schematic of experimental strategy to engineer a modular self-silencing ZFcharm Kv2 by using two distinct ZF domains. (H) Tuning of self-silencing kinetics by means of an allelic series of ZF3 backbone RtoA mutations. ZFcharm Kv2 and PrP expression were quantified 9 and 22 days after transduction. Data are mean \pm SD of $n = 2$ replicates.

and the other for target-gene repression (Fig. 5G). To comply with the AAV packaging limit, we optimized the construct to incorporate the Npu

intein strategy described above, in which a C-terminal N-extein and an N-terminal C-extein are fused to the CHARM domains and to each ZF,

respectively (Fig. 5G and fig. S10, A to C). We selected a previously characterized synthetic ZF, ZF3, for the self-silencing component (66).

Placing a single ZF3 binding site upstream of the EFS promoter resulted in complete self-silencing and minimal *Prnp* repression. We slowed the kinetics by cloning an allelic series of arginine-to-alanine (RtoA) mutations in the ZF3 backbone, with the added benefit of reducing off-target interactions (40, 78–80). Introducing two RtoA mutations in the ZF3 backbone slowed self-silencing enough for ZF-*Prnp* to first establish heritable *Prnp* repression without abrogating self-silencing (Fig. 5H). We also tested point mutations on the ZF3 DNA binding site, illustrating an alternative method to decrease the rate of self-silencing (fig. S10, D and E). Together, these results highlight the potential of self-silencing CHARMs to constrain transgene expression when using delivery modalities that result in sustained cargo expression.

Self-silencing CHARMs are functional in vivo

We packaged AAV capsids with the same self-silencing CHARM constructs tested in vitro (ZFcharm Kv1 and ZFcharm with DPM, SPM, SMM, and SCR self-silencing binding sites) to assess whether the self-silencing approach would translate in vivo (Fig. 6A). *Prnp* expression in the brain was strongly reduced across all conditions 6 weeks after AAV injection, with an inverse relationship between the speed of self-silencing and the degree of *Prnp* knockdown (Fig. 6, B and C). The KRBless self-silencing ZFcharm constructs again yielded similar results, indicating that DNA methylation alone is effective in suppressing episomal AAV transgenes in addition to endogenous genes (Fig. 6C).

To confirm that self-silencing CHARMs methylate their own promoter in vivo, we carried out clonal bisulfite sequencing on episomal AAV DNA extracted from brain homogenate. The SPM and DPM promoters acquired DNA methylation at the CpGs surrounding the TSS and next to the ZF binding site, matching the pattern observed in cultured cells (Fig. 5D; Fig. 6, D and E; and fig. S11, A and B). By contrast, the EFS promoter was completely unmethylated in single-stranded AAV genomic DNA extracted from ZFcharm Kv1-SPM AAV particles, indicating that self-silencing occurred after brain transduction and not during viral packaging (fig. S11C).

To assess the durability of *Prnp* repression following self-silencing in vivo, we quantified *Prnp* expression and AAV promoter methylation 13 weeks after injection of ZFcharm Kv1-packaged AAV (fig. S12A). The relationship between self-silencing efficiency and *Prnp* knockdown persisted, with no evidence of *Prnp* reactivation (fig. S12, B and C). *Prnp* promoter methylation was consistent with these results (fig. S13, A and B), and DNA methylation of the TSS driving ZFcharm expression in the SPM and DPM conditions was also maintained (fig. S12D). Collectively, our findings indicate that CHARM can be engi-

neered to silence itself in vivo after silencing its target. Additional optimization of self-silencing kinetics will further improve the balance between target repression and timely discontinuation of transgene expression, such as by modulating the number of CpG sites in the promoter (81). For instance, systems for small-molecule control of self-silencing, such as tamoxifen-induced nuclear localization of a synthetic ZF transcriptional repressor (66), could allow for more precise temporal control as well as compatibility with different DNA binding domains.

Discussion

The promise of genetic medicines has been limited by the challenges of delivering the large and elaborate effector complexes (e.g., Cas9-sgRNA ribonucleoproteins) typically required to mediate permanent changes to the genome or epigenome (82) as well as by toxicity and unintended consequences caused by repair of double-stranded breaks and single-stranded nicks. In this study, we have presented CHARM, a compact, programmable, and readily deliverable DNA methylation system capable of permanently silencing targeted genes with high specificity. CHARM leverages the existing cellular machinery, thus obviating the need to overexpress any catalytic domain. As such, these effectors are smaller and potentially less cytotoxic than existing technologies and do not rely on DNA sequence edits (83–90). Unlike genome-editing approaches that disrupt coding regions or splice sites (91, 92), CHARM does not lead to the permanent production of an altered mRNA encoding for a truncated protein.

The CHARM system can be readily encoded within the genome of AAV vectors when coupled with ZFPs, TALEs, or small CRISPR-Cas DNA binding domains. AAV-based delivery has been approved for indications in a variety of tissues, including the CNS, muscle, and blood (93). ZFcharm represents the first AAV-delivered tool capable of gene silencing through targeted DNA methylation. Specifically, we have shown in mice that the CHARM system can establish stable DNA methylation and transcriptional silencing of the prion protein in the majority of neurons, a postmitotic cell type, which argues for its utility in preventing other neurodegenerative diseases caused by a buildup of toxic protein aggregates (15, 16). The small size of ZFcharm enables a range of strategies for optimizing delivery and efficacy, which we have illustrated by developing modular and tunable self-silencing ZFcharms. This strategy can be extended to multiplexed targeting with up to three distinct ZFcharms or to the use of different promoters or 3'UTRs that drive robust cell type-specific expression. The major components of ZFcharm are either derived from or closely related to human proteins, so CHARM is expected to have reduced antigenic propensity,

especially in the context of time-limited expression. More in-depth in vivo toxicity and off-target analyses are critical next steps in developing CHARM as a therapeutic.

The dominant mechanism of Food and Drug Administration (FDA)-approved drugs is through inhibition of a target protein (94). Thus, although major challenges remain, long-term and reversible gene silencing is potentially applicable to prevent or treat a range of pathological processes. Additionally, silencing enhancers (32) could enable cell type-specific tuning of gene expression, and the relatively wide targeting window (~1 kb) of epigenetic silencers facilitates the use of single-nucleotide polymorphisms for allele-specific targeting. A wide variety of AAV capsid variants are in development with tropism for different tissues (95, 96), including a recently described engineered AAV capsid that crosses the blood-brain barrier by binding the human transferrin receptor, making it a promising candidate for human CNS delivery (97). In addition to AAVs, the compact and single-component nature of ZFcharm could greatly facilitate other delivery platforms. For example, the short mRNA of ZFcharm could be delivered by engineered virus-like particles or lipid nanoparticles (LNP) (82, 98, 99) without the need for co-delivery of guide RNAs and difficult-to-produce long mRNAs. This flexibility enables further applications of CHARM as both a therapeutic and a tool for studying chromatin biology.

Prion disease, which is currently untreatable and rapidly fatal, represents a promising area for the initial clinical development of AAV-delivered ZFcharms. Animal studies provide a strong rationale for the therapeutic targeting of the prion protein. Even after onset of symptoms, moderate decreases of PrP expression in neurons are sufficient to halt and even reverse the disease process (5), and complete inhibition of PrP expression is well-tolerated across several mammalian species (7–11). Our demonstration of >80% brainwide knockdown of PrP expression far exceeds the minimal knockdown required for a therapeutic effect—50% knockdown by an ASO extended survival with five different prion strains, and as little as 21% knockdown delayed symptom onset (100). Lastly, both the mouse and human *PRNP* genes can be readily and stably silenced, and homology between the *PRNP* promoter in humans and nonhuman primates could enable the design of cross-reactive ZFcharms for preclinical studies. Beyond the potential in treating prion disease, therapeutic targeting of *PRNP* will also provide practical experience on the benefits and unforeseen challenges of broader clinical applications of CHARM.

Materials and methods

Cell culture and cell-line generation

HEK293T (ATCC, CRL-3216) and Neuro-2a (N2a; ATCC, CCL-131) cells were cultured in

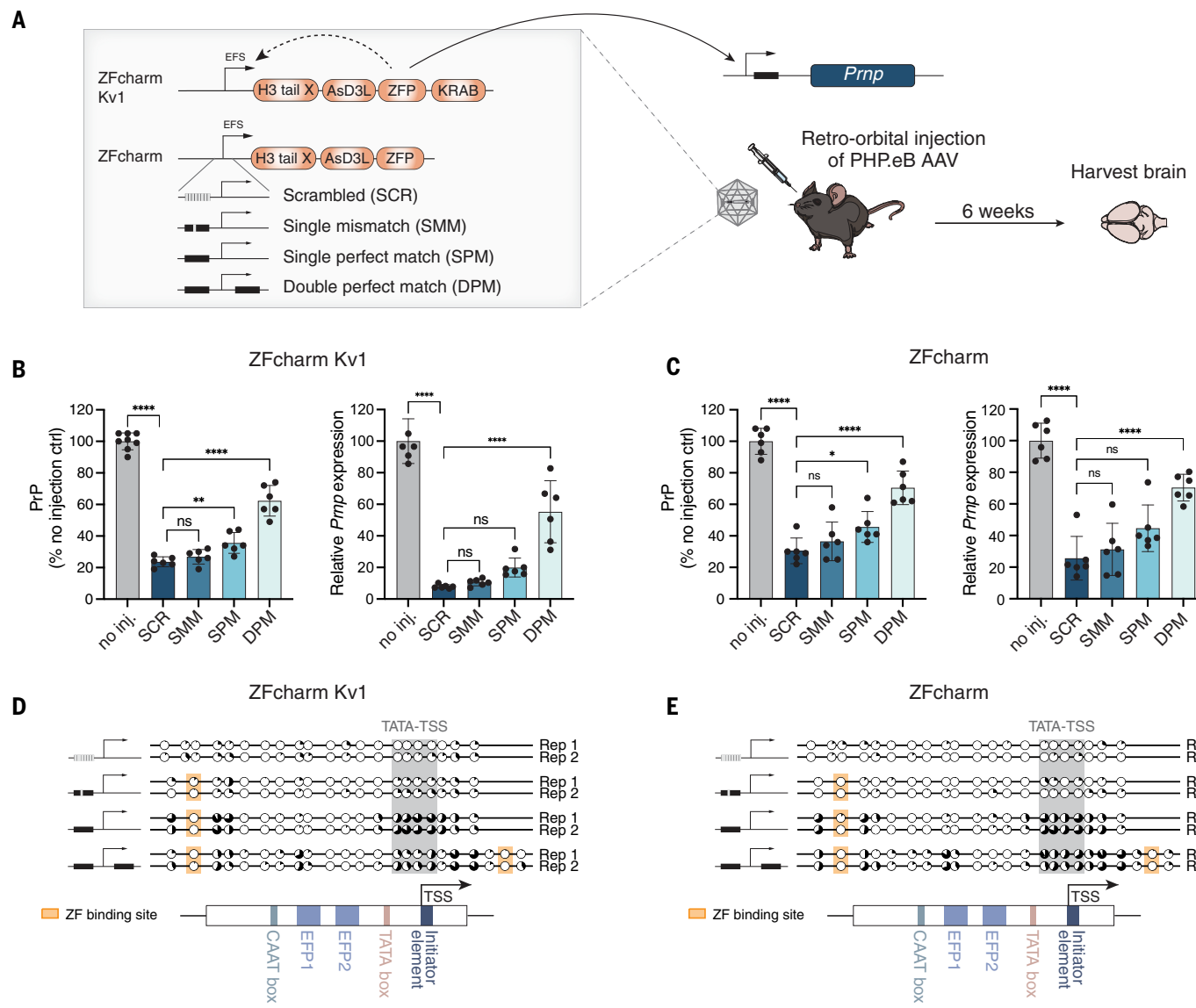


Fig. 6. Self-silencing ZFcharm is functional in vivo. (A) Schematic of experimental design. (B and C) PrP ELISA and *Prnp* RT-qPCR data generated from brain hemisphere homogenate 6 weeks after injection of 1.5×10^{13} vg/kg AAV. AAV capsids were packaged with self-silencing ZFcharm constructs containing (B) or lacking (C) the KRAB domain. Data are mean \pm SD of $n = 6$ to 8 replicates. Statistical analyses are one-way ANOVAs followed by Tukey's multiple comparisons test. * $P < 0.05$, ** $P < 0.005$, *** $P < 0.0005$,

**** $P < 0.0001$; ns, not significant. (D and E) Clonal bisulfite sequencing of the EFS promoter driving expression of self-silencing ZFcharm constructs containing (D) or lacking (E) the KRAB domain. The % 5mCpG (black) is calculated for each CpG site across PCR clones and depicted with pie charts. Sequence elements within the EFS promoter are shown in the schematic under the data. CpGs between the TATA box and TSS are highlighted in gray, and the ZF binding site is highlighted in orange.

Dulbecco's Modified Eagle Medium (DMEM) supplemented with 10% fetal bovine serum (FBS), 100 units/ml streptomycin, 100 μ g/ml penicillin, and 2 mM glutamine. Cells were passaged every 2 to 3 days using Trypsin-EDTA (0.25%). Cell lines were cultured at 37°C with 5% CO₂.

The mScarlet-*CLTA* cell line was generated by knocking in a 5' *mScarlet* tag at the *CLTA* locus. The sgRNA sequence targeting *CLTA* was ligated into pX458 (Addgene #48138) to generate the Cas9 + sgRNA plasmid. A double-

cut HDR donor plasmid with the *mScarlet* tag sequence flanked by 800 bp homology arms was cloned from a pUC19 backbone (Addgene #50005) using NEBuilder HiFi DNA Assembly (New England BioLabs, E2621L). Knockin efficiency was increased by flanking the donor sequence with sgRNA-PAM sequences used to target the *CLTA* locus to induce linearization after transfection (101). The HDR donor and Cas9 + sgRNA plasmids were co-transfected into HEK293T cells using TransIT-LT1 Transfection Reagent (Mirus Bio, 10767-122). mScarlet+ cells

were sorted by FACS 6 days after transfection and successful tag insertion was validated with PCR.

Plasmid design

Guide RNAs were designed using CRISPRick SpCas9 CRISPRi guide prediction software (102). The sgRNA-expressing lentiviral vectors were constructed by ligation of annealed oligonucleotides (IDT) downstream of the mU6 promoter using BstXI and BlpI restriction sites. The vector also expresses HaloTag7 to allow

for transfection and infection rate measurement by staining with Janelia Fluor HaloTag Ligands (Promega, GA1110). Cloning AAV plasmids and CHARM constructs was performed with eBlocks DNA fragments (IDT), oligonucleotides (IDT), or PCR amplicons produced from appropriate template sequences using Q5 Hot Start High-Fidelity 2x Master Mix (New England BioLabs, M0494L) or KOD Xtreme Hot Start DNA Polymerase (EMD Millipore, 719753). DNA fragments were cloned into restriction enzyme-digested plasmids using NEBuilder HiFi DNA Assembly (New England BioLabs, E2621L). All plasmids were sequence-confirmed by long-read whole-plasmid sequencing by Quintara Bio. Optimized CHARM sequences can be found in Table S2.

Plasmid transfection

Transient transfection experiments in N2a cells were performed in 6-well plates using TransIT-LT1 Transfection Reagent (Mirus Bio, 10767-122) and Opti-MEM Reduced Serum Medium (Thermo Fisher Scientific, 31985062). Cells at 70% confluence were transfected with 2.5 µg of plasmid. Cells co-transfected with plasmid encoding CRISPRoff or CRISPRi and plasmid encoding sgRNA were transfected with 1.7 µg and 800 ng, respectively. Transient transfection experiments in HEK293T cells were performed in 24-well plates using polyethylenimine (PEI). Cells at 70% confluence were transfected with 250 ng of plasmid. Transfected cells were sorted on TagBFP expression 2 days after transfection on a SONY MA900 and re-plated at a density of 120K cells/well in a 24-well plate. Cells were given 4 days to recover without changing media. Beginning at 6 days after transfection, cells were assessed for fluorescence markers using the Attune NxT Flow Cytometer and passaged at a 1:8 dilution every 2 days for the duration of the time course.

Lentiviral packaging and transduction

Lentiviral particles were produced by co-transfecting lentiviral transfer plasmids with standard packaging vectors psPAX2 (Addgene #12260) and pMD2.G (Addgene #12259) into HEK293T using FuGENE HD (Promega, PAE2311) or PEI. Media was replaced with fresh media supplemented with ViralBoost (Alstern, NCO966705) 6 hours after transfection. Viral supernatants were harvested 48 hours after transfection and flash-frozen. Lentiviral transductions were performed in polybrene-supplemented media (8 µg/ml). Media was replaced the following day and selection with 2 µg/ml puromycin was initiated 2 days after transduction.

PiggyBac transfection

The Super PiggyBac Transposase Expression Vector (System Biosciences, PB210PA-1) and CHARM-expressing *PiggyBac* transposon vector were co-transfected at a 1:10 molar ratio

into N2a cells using TransIT-LT1 Transfection Reagent (Mirus Bio, 10767-122). Selection with 2 µg/ml puromycin was initiated 2 days after transfection. Cells were assessed for ZFcharm Kv1 and PrP expression using immunofluorescence staining (see below) followed by flow cytometry using the Attune NxT Flow Cytometer.

Immunofluorescence staining

Staining for cell surface proteins PrP, CD51, CD81, and CD151 was performed on cells at 50 to 90% confluence in 24-well plates. Cells were resuspended in PBS using mechanical force and transferred to a 96-well V-bottom plate. Cells were incubated at 4°C in the dark for 30 min with the appropriate fluorophore-conjugated antibody (Alexa Fluor 647 6D11 anti-PrP, also called anti-CD230, Biolegend, 808007; APC anti-human CD81, Biolegend, 349509; APC anti-human CD55, Biolegend, 311311; APC anti-human CD151, Biolegend, 350405) at a concentration of 0.5 µg/ml. Cells were washed twice in PBS supplemented with 5% FBS and read out on the Attune NxT Flow Cytometer.

Cell viability staining

To assess cytotoxicity of the different epi-editors, HEK293T cells were transiently transfected with ZFP expressing constructs followed by FACS on TagBFP expression 2 days later. After recovering from FACS for 4 days, 1e6 cells were trypsinized, spun down at 400×g for 5 min, and resuspended in 1 ml of PBS. One µl of LIVE/DEAD Fixable Near-IR Dead Cell Stain for 633 or 635 nm excitation (Invitrogen L34975) dissolved in DMSO was added to the cells and kept on ice for 30 min protected from light. Cells were pelleted and washed with PBS twice followed by resuspension in 150 µl of PBS and flow cytometry on the Attune NxT Flow Cytometer. Total viable cells per 100 µl were counted based on near-IR (~780 nm) fluorescence.

Generation of genetic knockout cell lines

To knock out *DNMT3A* and *DNMT3B* in our mScarlet-CLTA reporter HEK293T cell line, we nucleofected Alt-R S.p. HiFi Cas9 Nuclease V3, 100 µg (IDT 1081060) complexed with guide RNA to form ribonucleoprotein (RNP). Guide RNAs designed using CRISPRick software (102) were formed by mixing 5 µl Alt-R CRISPR-Cas9 crRNA at 100 µM (IDT custom designs; table S1) and 5 µl Alt-R CRISPR-Cas9 tracrRNA at 100 µM (IDT 1072533) and boiling at 95°C for 5 min followed by cooling to room temperature. To make RNP, 1.4 µl of the 50 µM annealed guide RNA was mixed with 1 µl of the Cas9 nuclease (62 µM) and 0.6 µl of phosphate buffered saline to a final volume of 3 µl, which was incubated at room temperature for 20 min and then placed on ice until ready for electroporation. HEK293T reporter cells were dissociated

with trypsin and 1e6 cells were spun down. These were resuspended in Amaxa SF cell line 4D-nucleofector buffer with Cas9 RNP added and nucleofected in a 100 µl cuvette using program CM-130 following manufacturer's protocols (V4XC-2024, Lonza). Cells were immediately plated in a 6-well dish containing pre-warmed media (see culture conditions above). Knockout efficiency was determined by seeding cells in a 96-well plate and lysing with 200 µl QuickExtract DNA Extraction Solution (SS000035-D2, Biosearch Technologies) following manufacturer protocols. Two µl of cell lysate was used as a template for a 40 µl PCR using 2x Super Pfx Mastermix (CW2965, Cowin Biosciences) and the following primers: CAGC-CAGGCTCTAGACCCA (*DNMT3A*, Fwd), GGC-GGGGTCAATGTCTTCAGG (*DNMT3A*, Rev), TGGCAGGAAAAACCCCGTGT (*DNMT3B*, Fwd), and AGCCGTTCCCTATACATGAGTTCT (*DNMT3B*, Rev) (5' to 3') to generate a 715 bp amplicon for *DNMT3A* and a 700 bp amplicon for *DNMT3B*. PCRs were purified using QIAquick PCR Purification Kit (28104, Qiagen) and Sanger sequenced by Quintara Bio. Insertion/deletion (indel) frequencies were determined from Sanger traces using Synthego ICE analysis (<https://ice.synthego.com/#/>).

DNMT3L phylogeny construction

Genome-mining for *DNMT3L* orthologs and ancestral reconstructions was performed based on previously established methods (61). A list of ~200 *DNMT3L* orthologs was obtained by performing a BLASTP (103) search in the NCBI non-redundant protein sequences database, using the human and mouse *DNMT3L* amino acid sequences as a query, and removing sequences with >97% pairwise identity. A MAFFT multiple sequence alignment was performed using the FFT-NS-i (standard) strategy with a maximum of two iterations (104) and then used for phylogenetic tree construction implementing IQ-TREE software (105). With IQ-TREE we inferred the phylogenetic tree using the predicted best-fit model and ultrafast bootstrapping with 1000 replicates and optimized parameters. After visualization of the tree using the interactive tree of life (iTOL) v5 online tool (106), selected ancestral nodes were predicted with the IQ-TREE ASR function (105). Two dozen GenScript codon-optimized orthologs and ASRs were synthesized as DNA eBlocks (IDT). D3L sequences can be found in table S2. Custom Python scripts can be found in Zenodo (107).

TALE design

TALE DNA binding domains were constructed following published guidelines (108, 109). In brief, potential 18-nucleotide binding sites beginning with the invariable thymine were compiled from the mouse and human *PRNP* promoter regions and scored for specificity using nucleotide BLAST (103). Top candidates

were selected for synthesis in the chimerized TALE scaffold (63) using the following repeat variable diresidues (RVDs): HD for cytosine, NG for thymine, NI for adenine, NH for guanine, and G* for any possible 5-methyl-cytosine within a CpG dinucleotide. Each TALE was synthesized as eBlocks (IDT) in two halves which were cloned into a CHARM acceptor vector using NEBuilder HiFi DNA Assembly (New England BioLabs, E2621L). TALE sequences can be found in table S2.

Extraction of HMW gDNA

To extract high molecular weight (HMW) genomic DNA (gDNA) from cells for nanopore long-read sequencing analysis of CpG methylation, 10^6 cells were pelleted at $400 \times g$ for 5 min, rinsed with PBS, and pelleted again. Pellets were processed using the Monarch HMW DNA Extraction Kit for Cells & Blood (New England Biolabs, T3050L). To extract HMW gDNA from mouse brain tissue, two 150 μm coronal sections were cut from flash-frozen hemispheres embedded in optimal cutting temperature (O.C.T.) compound (see below) and collected in a single 1.5 ml Eppendorf tube. These were frozen at $-80^\circ C$ until ready for preparation. Prior to processing using the Monarch HMW DNA Extraction Kit for Tissue (New England Biolabs, T3060L), these sections were rinsed with ice-cold PBS twice and pelleted on a tabletop microcentrifuge (MyFuge 12 Mini Centrifuge, Benchmark Scientific C1012) to remove excess O.C.T. The gDNA extraction was performed following manufacturer instructions with slight modifications to maximize yield; three glass beads were used instead of two, and gDNA was eluted in 200 μl of water heated to $65^\circ C$. To concentrate the gDNA for Nanopore library preparation (to $\sim 5 \mu g$ DNA in $<24 \mu l$), gDNA in the eluate was precipitated by adding 2 μl 20 mg/ml glycogen (Thermo Scientific, R0561), 22 μl 3M pH 5.2 sodium acetate, and 155 μl pure room temperature isopropanol followed by mixing and centrifugation at $15,000 \times g$ for 20 min at $4^\circ C$. Supernatant was carefully decanted and DNA pellets were washed with 1 ml 70% ethanol and centrifuged at $15,000 \times g$ again for 10 min at $4^\circ C$. Supernatant was decanted and the pellet was air-dried for 10 min. The DNA pellet was redissolved in 25 μl water at $56^\circ C$ for 2 hours. Wide-bore pipette tips (Genesee Scientific, 22-427 and 22-424) were used for all gDNA handling steps to prevent shearing.

Target enrichment and Nanopore library preparation

Two upstream and two downstream guide RNAs were designed flanking the *PRNP* locus in a ~ 5 kb window using CHOPCHOPv3 (110). Alt-R CRISPR-Cas9 tracrRNA (IDT, 1072533) and custom Alt-R CRISPR-Cas9 crRNA (IDT) were annealed at 10 μM in nuclease-free duplex

buffer (IDT, 11-01-03-01). In a 1.5 ml Eppendorf tube, 79.2 μl of water was combined with 10 μl of reaction buffer (RB) from the Cas9 Sequence Kit Cas9 Sequencing Kit (Oxford Nanopore Technologies, SQK-CS9109), 10 μl of 10 μM pooled annealed guide RNAs, and 0.8 μl of 62 μM Cas9 nuclease (Alt-R S.p. HiFi Cas9 Nuclease V3, IDT 1081060) and was complexed at room temperature for 30 min before use. Prior to nanopore sequencing of native DNA molecules, the prion locus was enriched using 5 μg of input gDNA and prepared for sequencing following manufacturer's protocols (ONT, SQK-CS9109).

Nanopore sequencing

Target-enriched Nanopore libraries were loaded into a MinION Flow Cell R9.4.1 (ONT, FLO-MIN106D) after priming with the flow cell priming kit (ONT, EXP-FLP002) and sequenced on a MinION sequencing device (ONT, MIN-101B) with MinKNOW software (ONT, v23.04.6) using fast base calling combined with adaptive sampling to further enrich the target locus. Live base calling was enabled by hardware (13th Gen Intel Core i7-13700 2.10 GHz and 16 GB RAM) with a GPU (NVIDIA, GeForce RTX 3070) running Windows 11 Pro. Each library was sequenced in series, and the flow cell was washed using the flow cell wash kit (ONT, EXP-WSH004) between samples. Each flow cell could run three to four libraries before requiring replacement. Two biological replicates were sequenced for each sample type.

Nanopore base calling and data analysis

Base calling was performed on the raw FAST5 files with Guppy (ONT, v.6.5.7), using a configuration file for high-accuracy modified DNA base calling on an R9.4.1 pore at 450 bases s^{-1} . The resulting reads were then mapped to the GRCh38 (human) or GRCm39 (mouse) reference genome without alternate contigs using minimap2 v.2.26 with default settings for alignment of nanopore reads (-x map-ont). Reads were filtered based on reciprocal 90% coverage with the target locus using the bedtools v.2.31.0 intersect (-wo -f 0.9 -r) command. Filtered, sorted, and indexed bam output files were used for methylation visualization (see below) or further processed using modkit tools (ONT, <https://github.com/nanoporetech/modkit>) and custom python scripts implementing NumPy v.1.26.3, Pandas v.2.2.0, and Seaborn v.0.13.2 for Pearson correlation and average methylation plots. Virtual environment files and custom Python scripts can be found in Zenodo (107).

Visualization of DNA methylation on individual nanopore reads

Output bam files with read names numbered by average methylation were indexed and loaded into Integrative Genomics Viewer (111) v2.16.2

with the following settings: squished, small indel threshold <100 bp, hide mismatched bases, hide insertion markers, quick consensus mode, color by 5mC, sort by Read Name, Reverse Sort. To change colors to black (unmethylated) and blue (methylated), exported PNG files were adjusted with an Adobe Photoshop 2024 batch processing script for consistency.

RNA-seq analysis

N2a cells were maintained for 28 days post lentiviral transduction of ZFchrm Kv1 or CRISPRchrm Kv1 constructs. CRISPRchrm Kv1 was introduced into cells already expressing either a non-targeting sgRNA or a sgRNA targeting *Prnp*. An empty lentiviral vector was used as a no-editor control. Each transduction was done in triplicate. Cells were dislodged from 6-well plates using Trizol and total RNA was extracted using the Direct-zol RNA Miniprep Kit (Zymo, R2051). Libraries were prepared using the KAPA RNA HyperPrep Kit with RiboErase (HMR) (Roche, KK8560) and sequenced as 50 bp single-end reads on a NovaSeq 6000 (Illumina). Raw sequencing reads were aligned to the mouse genome (mm39) using STAR 2.7.1a and quantified using featureCounts 1.6.2 (112). Differential expression analysis was carried out using DESeq2 (113) using default parameters. The lfcShrink function was applied using the apeglim shrinkage estimator. Sequencing data are available on GEO (GSE255987).

Clonal bisulfite sequencing

Clonal bisulfite sequencing (32) of the EFS promoter was performed on (i) genomic DNA extracted from lentivirally transduced N2a cells, (ii) double-stranded AAV genomes extracted from brain homogenate, or (iii) single-stranded AAV genomes extracted from viral particles. N2a genomic DNA was extracted using the PureLink Genomic DNA Mini Kit (Invitrogen, K182001). AAV episomal DNA was obtained through Trizol-Chloroform extraction from brain homogenate followed by treatment with T5 exonuclease (New England BioLabs, M0663S) and RNase Cocktail Enzyme Mix (Thermo Fisher Scientific, AM2288). To extract single-stranded AAV DNA, viral particles were treated with TurboNuclease (MilliporeSigma, T4330) to digest contaminating plasmid DNA and then with Proteinase K to digest viral capsids. Both double- and single-stranded AAV DNA was purified with the DNA Clean & Concentrator-5 Kit (Zymo, 11-302B). Bisulfite conversion was performed on 100 to 500 ng DNA using the EZ DNA Methylation Lightning Kit (Zymo, D5001). Purified bisulfite-converted DNA was amplified with forward primer GAGTGGTTAATTTATTATTAGGGGT (5' to 3') and reverse primer TTTCTAACAAATTATTTAATCCTAACCA (5' to 3') using EpiMark Hot Start Taq (New England BioLabs, M0490S), and purified using a QIAquick PCR Purification

Kit (QIAGEN, 28104). Amplicons were cloned into pCR2.1-TOPO Vector using a TOPO TA Cloning Kit (Invitrogen, 451641) and transformed into Stellar Competent *E. coli* Cells (Takara Bio, 636766). Cells were plated on plates supplemented with carbenicillin, X-gal, and IPTG for blue-white screening. Colonies were sequenced by Sanger sequencing and reads were processed for display using QUMA software (114).

AAV production and titering

Recombinant AAVs (AAV-PHP.eB) were produced in suspension HEK293T cells, using F17 media (Thermo Fisher, A138501). Cell suspensions were incubated at 37°C, 8% CO₂, 80 RPM, 24 hours before transfection, cells were seeded in 500 to 1000 ml at ~1 million cells/ml. The day after, cells (~2 million cells/ml) were transfected with pHelper, pRepCap, and pTransgene (2:1:1 ratio, 2 µg total DNA per million cells) using Transport 5 transfection reagent (Polysciences, 26008-50) with a 2:1 PEI:DNA ratio. Three days after transfection, cells were pelleted at 2000 RPM for 12 min into Nalgene conical bottles. The supernatant was discarded, and cell pellets were stored at -20°C until purification. Each pellet, corresponding to 500 ml of cell culture, was resuspended in 14 ml of 500 mM NaCl, 40 mM Tris-base, 10 mM MgCl₂, with Salt Active Nuclease (ArcticZymes, #70920-202) at 100 U/ml. Afterwards, the lysate was clarified at 5000 RCF for 20 min and loaded onto a density step gradient containing OptiPrep (Cosmo Bio, AXS-1114542) at 60, 40, 25, and 15% at a volume of 6, 6, 8, and 5 ml, respectively, in OptiSeal tubes (Beckman, 342414). The step gradients were spun in a Beckman Type 70ti rotor (Beckman, 337922) in a Sorvall WX+ ultracentrifuge (Thermo Scientific, 75000090) at 67,000 RPM for 75 min at 18°C. Afterwards, ~4.5 ml of the 40 to 60% interface was extracted using a 16-gauge needle, filtered through a 0.22 µm PES filter, buffer exchanged with 100K MWCO protein concentrators (Thermo Scientific, 88532) into PBS containing 0.001% Pluronic F-68, and concentrated down to a volume of 200 to 1000 µl. The concentrated virus was filtered through a 0.22 µm PES filter and stored at 4°C or -80°C.

To determine AAV titers, 5 µl of each purified virus library was incubated with 100 µl of an endonuclease cocktail consisting of 1000U/ml TurboNuclease (Sigma T4330-50KU) with 1X DNase I reaction buffer (New England BioLabs, B0303S) in UltraPure DNase/RNase-Free distilled water at 37°C for 1 hour. Next, the endonuclease solution was inactivated by adding 5 µl of 0.5 M EDTA, pH 8.0 (Thermo Fisher Scientific, 15575020) and incubated at room temperature for 5 min and then at 70°C for 10 min. To release the encapsidated AAV genomes, 120 µl of a Proteinase K cocktail consisting of 1 M NaCl, 1% N-lauroylsarcosine, 100 µg/ml Proteinase K

(QIAGEN, 19131) in UltraPure DNase/RNase-Free distilled water was added to the mixture and incubated at 56°C for 2 to 16 hours. The Proteinase K-treated samples were then heat-inactivated at 95°C for 10 min. The released AAV genomes were serially diluted between 460 to 4,600,000X in dilution buffer consisting of 10X PCR Buffer (Thermo Fisher Scientific, N8080129), 2 µg/ml sheared salmon sperm DNA (Thermo Fisher Scientific, AM9680), and 0.05% Pluronic F68 (Thermo Fisher Scientific, 24040032) in UltraPure Water (Thermo Fisher Scientific). Two µl of the diluted samples were used as input in a ddPCR supermix (Bio-Rad, 1863023). Primers and probes, targeting the ITR region, were used for titration at a final concentration of 900 nM and 250 nM (ITR2_-Forward: 5'-GGAACCCCTAGTGATGGAGTT-3'; ITR2_-Reverse: 5'-CGGCCTCAGTGAGCGA-3'). The droplets were transferred to the thermocycler and cycled according to the manufacturer's protocol with an annealing/extension of 58°C for 1 min. Finally, droplets were read on a QX100 Droplet Digital System to determine titers.

Mice

All in vivo experiments were approved by the Institutional Animal Care and Use Committee of the Broad Institute (Protocol #0162-05-16-2, most recent approval date: 2024-01-03) and were performed in accordance with the National Institutes of Health *Guide for the Care and Use of Laboratory Animals*. Experiments in this study used 192 C57BL/6N mice (90 female, 102 male) obtained from Charles River Laboratories. Unless otherwise noted, mice were between 5 to 8 weeks old at the time of AAV injections.

Intravenous AAV injection

Mice were anesthetized using inhaled isoflurane at 1 to 3%. AAV vectors (0.75×10^{13} , 1.5×10^{13} , or 3×10^{13} vg/kg, ~100 µl injection volume) were administered intravenously into the right retro-orbital sinus of the animal using a 300 µl insulin syringe with a 31G needle (328438, Becton Dickinson, USA) following established protocols (64, 115). One drop of 0.5% propracaine (07-892-9554, Patterson Veterinary, USA) was applied topically to the eye immediately following injection. Mice were euthanized using CO₂ inhalation at time points of 6 or 13 weeks after injection, following which the brains were harvested and cut in half. One hemisphere was placed in a microtube and flash-frozen on dry ice for ELISA (see below), while the other hemisphere was prepared for histological analysis. In brief, a small amount of optimal cutting temperature (OCT) compound (Tissue-Tek 4583, Sakura, USA) was placed into a 15 by 15 by 5 mm cryomold (Tissue-Tek 4566, Sakura, USA), the hemisphere was placed cut side down into the mold, and fully covered with additional OCT compound prior to being flash-frozen on

dry ice. All samples were stored at -80°C until further processing.

Mouse perfusions

Mice were deeply anesthetized under 2 to 5% isoflurane and 0.5 to 1 LPM oxygen in an induction chamber. Mice were then transferred to a nose cone providing 2 to 5% isoflurane and 0.5 to 1 LPM oxygen. Anesthesia depth was validated with lack of bilateral toe pinch prior to the start of the surgical procedure. Mice were continuously monitored throughout the procedure for any signs of responsiveness. Paw color and respiration rate were monitored at all times during anesthesia. Once anesthesia was stable and at an acceptable plane for surgery (based on lack of a toe-pinch and eye blink response, and stable slow respiratory rate), an incision was made through the skin below the ribcage and blunt dissection scissors were used to separate the outer layers of skin from the cavity wall. A mid-sternal thoracotomy was then performed to expose the heart and great vessels. Perfusate was delivered using a needle through the left ventricle and an incision was made in the right atrium to provide an outflow for blood and perfused fluids.

Perfusion was carried out with ice-cold saline solution followed by phosphate buffered saline containing 4% paraformaldehyde (PFA). Perfusion was complete when outflow perfusate showed no visual trace of blood, and the animal had no cardiac or respiratory activity. Mice were decapitated prior to brain dissection.

Brain homogenization

One hemisphere was homogenized at 10% wt/vol in cold 0.2% CHAPS solution prepared in 1X PBS with 1 tablet protease inhibitor (Roche Complete 4693159001, Millipore Sigma, USA) per 10 ml in 7 ml tubes pre-loaded with zirconium oxide beads (Precellys, Bertin, USA), using 3 × 40 s pulses on a Bertin MiniLysis Homogenizer (Bertin, USA). Homogenate was aliquoted into 40 µl aliquots for protein analysis and 300 µl aliquots for qPCR analysis, and stored at -80°C until further analysis.

Protein analysis

PrP concentration in the brain was quantified using a previously published PrP ELISA (70). Briefly, the assay uses EP1802Y antibody (ab52604, Abcam, USA) for capture and biotinylated 8H4 antibody (ab61409, Abcam, USA) for detection, with streptavidin-HRP (Pierce High Sensitivity, 21130, Thermo Fisher Scientific, USA) and TMB substrate (7004P4, Cell Signaling Technology, USA). Recombinant mouse PrP (MoPrP23-231) prepared as described (116) was used for a standard curve. Protein knockdown was calculated by dividing the concentration of residual PrP in each treatment brain, by the mean concentration of residual PrP in the saline control brains from the same time point.

RT-qPCR

Mouse *Prnp* RNA was quantified using RT-qPCR. RNA extracts were treated with DNase I (New England BioLabs, M0303S). Library preparation was performed using the RevertAid First Strand Synthesis Kit (Thermo Fisher Scientific, K1691). Taqman qPCR (Thermo Fisher Scientific, 4331182) was performed on cDNA samples using the QuantStudio 7 Flex (Applied Biosystems). $\Delta\Delta Ct$ values were calculated based on the amplification of *Gapdh*, and normalized to the mean of the no injection controls. Probe and quencher sequences were purchased from Fisher Scientific as pre-mixed Gene Expression Assays (*Gapdh* control, ID Mm99999915_g1; *Prnp* target, ID Mm07296968_m1).

Tissue processing and sectioning

Whole mouse brains harvested from perfused mice were incubated overnight at 4°C in 4% PFA. Fixed brains were then washed in 1X PBS and dehydrated overnight at 4°C in 30% sucrose, followed by a second overnight incubation at 4°C in a 1:1 mixture of 30% sucrose and O.C.T. compound (Tissue-Tek, 4583). Dehydrated brains were placed in cryomolds containing O.C.T. and snap-frozen in liquid nitrogen-chilled isopentane. 10 µm coronal brain sections were cut using a Leica CM3050 S Research Cryostat and placed on SuperFrost Plus slides (VWR, 48311-703). Brains used to extract DNA for nanopore long-read sequencing were harvested from non-perfused mice and directly embedded in O.C.T. before freezing on dry ice. These were cut into 150 µm sections using a Leica CM3050 S Research Cryostat and stored in tubes at -80°C before use.

HCR RNA-FISH

Coronal brain sections on SuperFrost Plus slides were immersed in 4% PFA at 4°C for 15 min and then sequentially immersed in 50% ethanol, 70% ethanol, 100% ethanol, and 1X PBS at room temperature for 5 min. A hydrophobic barrier was drawn around the tissue using an ImmEdge Hydrophobic Barrier Pen (Vector Laboratories, 101098-065). Third-generation multiplexed HCR RNA-FISH was performed as previously described (117). Briefly, tissue samples were pre-hybridized in hybridization buffer (Molecular Instruments) at 37°C for 10 min and then incubated in a 37°C humidified chamber overnight with split-initiator probes hybridizing to the *Prnp* and *Uchl1* mRNA transcripts diluted to a concentration of 4 nM in Hybridization Buffer. Split-initiator probes were purchased from Molecular Technologies. The slides were then immersed in 75, 50, and 25% probe wash buffer (Molecular Instruments) solutions at 37°C for 15 min, followed by two incubations in 5X SSCT, one for 15 min at 37°C and another for 5 min at room temperature. Tissue sections were then equilibrated in amplification

buffer (Molecular Instruments) for 30 min at room temperature. Separately, metastable fluorescent hairpins conjugated to Alexa Fluor 647 and Alexa Fluor 546 were snap-cooled and diluted to 60 nM in amplification buffer. Samples were incubated in hairpin solution overnight in a dark humidified chamber at room temperature. Excess hairpin amplifiers were removed the next day in 5X SSCT at room temperature before staining with 1 µg/ml DAPI for 10 min, washing again in 5X SSCT, and mounting in VECTASHIELD PLUS Antifade Mounting Medium (Vector Laboratories, H-1900). Brain sections were imaged as z-stack tile scans on a Zeiss LSM 980 with Airyscan 2 Laser Scanning Confocal with a 20X objective.

Image analysis

Maximum orthogonal projections and stitching of z-stack tile scales was performed using ZEN Blue software (Zeiss). Cell detection and classification was carried out using QuPath software v0.5.0 (71). Briefly, cells were detected using QuPath's cell detection tool on the DAPI channel (cell expansion = 4 µm). QuPath's built-in machine learning classification tool was used to detect neurons (using *Uchl1*-Alexa Fluor 647 signal) and *Prnp*+ cells (using *Prnp*-Alexa Fluor 546 signal). Multiple images were used to train the classifiers. Zoomed-in images of brain regions were median filtered using Fiji software v2.9.0 (118).

Statistical analyses

All statistical tests performed in this study are indicated in the figure legends.

Note added in proof: During the review process, Cappelluti *et al.* reported efficient and durable DNA methylation-based silencing of *Pcsk9* in mouse liver using LNP-based delivery (119).

REFERENCES AND NOTES

- S. B. Prusiner, Prions. *Proc. Natl. Acad. Sci. U.S.A.* **95**, 13363–13383 (1998). doi: 10.1073/pnas.95.23.13363; pmid: 9811807
- S. M. Vallabh, E. V. Minikel, S. L. Schreiber, E. S. Lander, Towards a treatment for genetic prion disease: Trials and biomarkers. *Lancet Neurol.* **19**, 361–368 (2020). doi: 10.1016/S1474-4422(19)30403-X; pmid: 32199098
- R. A. Maddox *et al.*, Prion disease incidence in the United States: 2003–2015. *Neurology* **94**, e153–e157 (2020). doi: 10.1212/WNL.00000000000008680; pmid: 31757870
- H. Büeler *et al.*, Mice devoid of PrP are resistant to scrapie. *Cell* **73**, 1339–1347 (1993). doi: 10.1016/0092-8674(93)90360-3; pmid: 8100741
- G. Mallucci *et al.*, Depleting neuronal PrP in prion infection prevents disease and reverses spongiosis. *Science* **302**, 871–874 (2003). doi: 10.1126/science.1090187; pmid: 14593181
- G. J. Raymond *et al.*, Antisense oligonucleotides extend survival of prion-infected mice. *JCI Insight* **5**, e131175 (2019). doi: 10.1172/jci.insight.131175; pmid: 31361599
- H. Büeler *et al.*, Normal development and behaviour of mice lacking the neuronal cell-surface PrP protein. *Nature* **356**, 577–582 (1992). doi: 10.1038/356577a0; pmid: 1373228
- S. L. Benestad, L. Austbø, M. A. Tranulis, A. Espenes, I. Olsaker, Healthy goats naturally devoid of prion protein. *Vet. Res.* **43**, 87 (2012). doi: 10.1186/1297-9716-43-87; pmid: 23249298
- J. A. Richt *et al.*, Production of cattle lacking prion protein. *Nat. Biotechnol.* **25**, 132–138 (2007). doi: 10.1038/nbt1271; pmid: 17195841
- E. V. Minikel *et al.*, Evaluating drug targets through human loss-of-function genetic variation. *Nature* **581**, 459–464 (2020). doi: 10.1038/s41586-020-2267-z; pmid: 32461653
- E. V. Minikel *et al.*, Quantifying prion disease penetrance using large population control cohorts. *Sci. Transl. Med.* **8**, 322ra9 (2016). doi: 10.1126/scitranslmed.aad5169; pmid: 26791950
- A. Küfer *et al.*, The prion protein is an agonistic ligand of the G protein-coupled receptor Adgrg6. *Nature* **536**, 464–468 (2016). doi: 10.1038/nature19312; pmid: 27501152
- F. S. Skedros *et al.*, Demyelinating polyneuropathy in goats lacking prion protein. *FASEB J.* **34**, 2359–2375 (2020). doi: 10.1096/fj.201920588R; pmid: 31907995
- J. Bremer *et al.*, Axonal prion protein is required for peripheral myelin maintenance. *Nat. Neurosci.* **13**, 310–318 (2010). doi: 10.1038/nn.2483; pmid: 20998419
- B. Frost, M. I. Diamond, Prion-like mechanisms in neurodegenerative diseases. *Nat. Rev. Neurosci.* **11**, 155–159 (2010). doi: 10.1038/nrn2786; pmid: 20029438
- F. Saudou, S. Humbert, The Biology of Huntingtin. *Neuron* **89**, 910–926 (2016). doi: 10.1016/j.neuron.2016.02.003; pmid: 26938440
- J. M. Dantart *et al.*, Efficacy of anti-amyloid-β monoclonal antibody therapy in early Alzheimer’s disease: A systematic review and meta-analysis. *Neurol. Sci.* **45**, 2461–2469 (2024). doi: 10.1007/s10072-023-07194-w; pmid: 37978096
- L. A. Gilbert *et al.*, CRISPR-mediated modular RNA-guided regulation of transcription in eukaryotes. *Cell* **154**, 442–451 (2013). doi: 10.1016/j.cell.2013.06.044; pmid: 23849981
- L. Holtzman, C. A. Gersbach, Editing the Epigenome: Reshaping the Genomic Landscape. *Annu. Rev. Genomics Hum. Genet.* **19**, 43–71 (2018). doi: 10.1146/annurev-genom-083117-021632; pmid: 29852072
- J. H. Goell, I. B. Hilton, CRISPR/Cas-Based Epigenome Editing: Advances, Applications, and Clinical Utility. *Trends Biotech.* **39**, 678–691 (2021). doi: 10.1016/j.tibtech.2020.10.012; pmid: 33972106
- M. Nakamura, Y. Gao, A. A. Dominguez, L. S. Qi, CRISPR technologies for precise epigenome editing. *Nat. Cell Biol.* **23**, 11–22 (2021). doi: 10.1038/s41556-020-00620-7; pmid: 33420494
- P. I. Thakore, J. B. Black, I. B. Hilton, C. A. Gersbach, Editing the epigenome: Technologies for programmable transcription and epigenetic modulation. *Nat. Methods* **13**, 127–137 (2016). doi: 10.1038/nmeth.3733; pmid: 26820547
- M. Park, A. J. Keung, A. S. Khalil, The epigenome: The next substrate for engineering. *Genome Biol.* **17**, 183 (2016). doi: 10.1186/s13059-016-1046-5; pmid: 27582168
- G. Kungulowski, A. Jeltsch, Epigenome Editing: State of the Art, Concepts, and Perspectives. *Trends Genet.* **32**, 101–113 (2016). doi: 10.1016/j.tig.2015.12.001; pmid: 26732754
- X. S. Liu *et al.*, Editing DNA Methylation in the Mammalian Genome. *Cell* **167**, 233–247.e17 (2016). doi: 10.1016/j.cell.2016.08.056; pmid: 27662091
- J. I. McDonald *et al.*, Reprogrammable CRISPR/Cas9-based system for inducing site-specific DNA methylation. *Biol. Open* **5**, 866–874 (2016). doi: 10.1242/bio.019067; pmid: 27170255
- H. O’Geen *et al.*, dCas9-based epigenome editing suggests acquisition of histone methylation is not sufficient for target gene repression. *Nucleic Acids Res.* **45**, 9901–9916 (2017). doi: 10.1093/nar/gkx578; pmid: 28973434
- A. Amabile *et al.*, Inheritable Silencing of Endogenous Genes by Hit-and-Run Targeted Epigenetic Editing. *Cell* **167**, 219–232.e14 (2016). doi: 10.1016/j.cell.2016.09.006; pmid: 27662090
- T. Mlambo *et al.*, Designer epigenome modifiers enable robust and sustained gene silencing in clinically relevant human cells. *Nucleic Acids Res.* **46**, 4456–4468 (2018). doi: 10.1093/nar/gky171; pmid: 29538770
- D. Hofacker *et al.*, Engineering of Effector Domains for Targeted DNA Methylation with Reduced Off-Target Effects. *Int. J. Mol. Sci.* **21**, 502 (2020). doi: 10.3390/ijms21020502; pmid: 31941101
- S. Kalusch *et al.*, Evidence that direct inhibition of transcription factor binding is the prevailing mode of gene and repeat repression by DNA methylation. *Nat. Genet.* **54**, 1895–1906 (2022). doi: 10.1038/s41588-022-01241-6; pmid: 36471082
- J. K. Nuñez *et al.*, Genome-wide programmable transcriptional memory by CRISPR-based epigenome editing.

- Cell* **184**, 2503–2519.e17 (2021). doi: [10.1016/j.cell.2021.03.025](https://doi.org/10.1016/j.cell.2021.03.025); pmid: [33838111](https://pubmed.ncbi.nlm.nih.gov/33838111/)
33. R. C. Challis *et al.*, Systemic AAV vectors for widespread and targeted gene delivery in rodents. *Nat. Protoc.* **14**, 379–414 (2019). doi: [10.1038/s41596-018-0097-3](https://doi.org/10.1038/s41596-018-0097-3); pmid: [30626963](https://pubmed.ncbi.nlm.nih.gov/30626963/)
34. C. T. Charlesworth *et al.*, Identification of preexisting adaptive immunity to Cas9 proteins in humans. *Nat. Med.* **25**, 249–254 (2019). doi: [10.1038/s41591-018-0326-x](https://doi.org/10.1038/s41591-018-0326-x); pmid: [30692695](https://pubmed.ncbi.nlm.nih.gov/30692695/)
35. D. Ren, S. Fisson, D. Dalkara, D. Ail, Immune Responses to Gene Editing by Viral and Non-Viral Delivery Vectors Used in Retinal Gene Therapy. *Pharmaceutics* **14**, 1973 (2022). doi: [10.3390/pharmaceutics14091973](https://doi.org/10.3390/pharmaceutics14091973)
36. D. L. Wagner *et al.*, High prevalence of Streptococcus pyogenes Cas9-reactive T cells within the adult human population. *Nat. Med.* **25**, 242–248 (2019). doi: [10.1038/s41591-018-0204-6](https://doi.org/10.1038/s41591-018-0204-6); pmid: [30374197](https://pubmed.ncbi.nlm.nih.gov/30374197/)
37. C. O. Pabo, E. Peisach, R. A. Grant, Design and selection of novel Cys2His2 zinc finger proteins. *Annu. Rev. Biochem.* **70**, 313–340 (2001). doi: [10.1146/annurev.biochem.70.1.313](https://doi.org/10.1146/annurev.biochem.70.1.313); pmid: [11395410](https://pubmed.ncbi.nlm.nih.gov/11395410/)
38. M. L. Maeder *et al.*, Rapid “open-source” engineering of customized zinc-finger nucleases for highly efficient gene modification. *Mol. Cell* **31**, 294–301 (2008). doi: [10.1016/j.molcel.2008.06.016](https://doi.org/10.1016/j.molcel.2008.06.016); pmid: [1867511](https://pubmed.ncbi.nlm.nih.gov/1867511/)
39. M. S. Bhakta, D. J. Segal, The generation of zinc finger proteins by modular assembly. *Methods Mol. Biol.* **649**, 3–30 (2010). doi: [10.1007/978-1-60761-753-2_1](https://doi.org/10.1007/978-1-60761-753-2_1); pmid: [20680825](https://pubmed.ncbi.nlm.nih.gov/20680825/)
40. D. M. Ichikawa *et al.*, A universal deep-learning model for zinc finger design enables transcription factor reprogramming. *Nat. Biotechnol.* **41**, 1117–1129 (2023). doi: [10.1038/s41587-022-01624-4](https://doi.org/10.1038/s41587-022-01624-4); pmid: [36702896](https://pubmed.ncbi.nlm.nih.gov/36702896/)
41. R. R. Beerli, C. F. Barbas3rd, Engineering polydactyl zinc-finger transcription factors. *Nat. Biotechnol.* **20**, 135–141 (2002). doi: [10.1038/nbt0202-135](https://doi.org/10.1038/nbt0202-135); pmid: [11821858](https://pubmed.ncbi.nlm.nih.gov/11821858/)
42. J. D. Sander *et al.*, Selection-free zinc-finger-nuclease engineering by context-dependent assembly (CoDA). *Nat. Methods* **8**, 67–69 (2011). doi: [10.1038/nmeth.1542](https://doi.org/10.1038/nmeth.1542); pmid: [2151135](https://pubmed.ncbi.nlm.nih.gov/2151135/)
43. D. E. Paschon *et al.*, Diversifying the structure of zinc finger nucleases for high-precision genome editing. *Nat. Commun.* **10**, 1133 (2019). doi: [10.1038/s41467-019-08867-x](https://doi.org/10.1038/s41467-019-08867-x); pmid: [30850604](https://pubmed.ncbi.nlm.nih.gov/30850604/)
44. B. Zeitler *et al.*, Allele-selective transcriptional repression of mutant HTT for the treatment of Huntington’s disease. *Nat. Med.* **25**, 1131–1142 (2019). doi: [10.1038/s41591-019-0478-3](https://doi.org/10.1038/s41591-019-0478-3); pmid: [31263285](https://pubmed.ncbi.nlm.nih.gov/31263285/)
45. S. Wegmann *et al.*, Persistent repression of tau in the brain using engineered zinc finger protein transcription factors. *Sci. Adv.* **7**, eabe1611 (2021). doi: [10.1126/sciadv.abe1611](https://doi.org/10.1126/sciadv.abe1611); pmid: [33741591](https://pubmed.ncbi.nlm.nih.gov/33741591/)
46. A. M. Moreno *et al.*, Long-lasting analgesia via targeted in situ repression of Nav1.7 in mice. *Sci. Transl. Med.* **13**, eaay9056 (2021). doi: [10.1126/scitranslmed.aay9056](https://doi.org/10.1126/scitranslmed.aay9056); pmid: [33692134](https://pubmed.ncbi.nlm.nih.gov/33692134/)
47. A. Tanenhaus *et al.*, Cell-Selective Adeno-Associated Virus-Mediated SCN1A Gene Regulation Therapy Rescues Mortality and Seizure Phenotypes in a Dravet Syndrome Mouse Model and Is Well Tolerated in Nonhuman Primates. *Hum. Gene Ther.* **33**, 579–597 (2022). doi: [10.1089/hum.2022.037](https://doi.org/10.1089/hum.2022.037); pmid: [35435735](https://pubmed.ncbi.nlm.nih.gov/35435735/)
48. M. V. C. Greenberg, D. Bourc’his, The diverse roles of DNA methylation in mammalian development and disease. *Nat. Rev. Mol. Cell Biol.* **20**, 590–607 (2019). doi: [10.1038/s41580-019-0159-6](https://doi.org/10.1038/s41580-019-0159-6); pmid: [31399642](https://pubmed.ncbi.nlm.nih.gov/31399642/)
49. Y. H. Huang *et al.*, DNA epigenome editing using CRISPR-Cas SunTag-directed DNMT3a. *Genome Biol.* **18**, 176 (2017). doi: [10.1186/s13059-017-1306-z](https://doi.org/10.1186/s13059-017-1306-z); pmid: [28923089](https://pubmed.ncbi.nlm.nih.gov/28923089/)
50. U. Rothbauer *et al.*, Targeting and tracing antigens in live cells with fluorescent nanobodies. *Nat. Methods* **3**, 887–889 (2006). doi: [10.1038/nmeth953](https://doi.org/10.1038/nmeth953); pmid: [17060912](https://pubmed.ncbi.nlm.nih.gov/17060912/)
51. M. V. Van, T. Fujimori, L. Bintu, Nanobody-mediated control of gene expression and epigenetic memory. *Nat. Commun.* **12**, 537 (2021). doi: [10.1038/s41467-020-20757-1](https://doi.org/10.1038/s41467-020-20757-1); pmid: [33483487](https://pubmed.ncbi.nlm.nih.gov/33483487/)
52. T. H. Xu *et al.*, Structure of nucleosome-bound DNA methyltransferases DNMT3A and DNMT3B. *Nature* **586**, 151–155 (2020). doi: [10.1038/s41586-020-2747-1](https://doi.org/10.1038/s41586-020-2747-1); pmid: [32968275](https://pubmed.ncbi.nlm.nih.gov/32968275/)
53. X. Guo *et al.*, Structural insight into autoinhibition and histone H3-induced activation of DNMT3A. *Nature* **517**, 640–644 (2015). doi: [10.1038/nature13899](https://doi.org/10.1038/nature13899); pmid: [25383530](https://pubmed.ncbi.nlm.nih.gov/25383530/)
54. B. Z. Li *et al.*, Histone tails regulate DNA methylation by allosterically activating de novo methyltransferase. *Cell Res.* **21**, 1172–1181 (2011). doi: [10.1038/cr.2011.92](https://doi.org/10.1038/cr.2011.92); pmid: [21606950](https://pubmed.ncbi.nlm.nih.gov/21606950/)
55. Y. Zhang *et al.*, Chromatin methylation activity of Dnmt3a and Dnmt3a/3L is guided by interaction of the ADD domain with the histone H3 tail. *Nucleic Acids Res.* **38**, 4246–4253 (2010). doi: [10.1093/nar/gkq147](https://doi.org/10.1093/nar/gkq147); pmid: [20223770](https://pubmed.ncbi.nlm.nih.gov/20223770/)
56. N. Z. Lue *et al.*, Base editor scanning charts the DNMT3A activity landscape. *Nat. Chem. Biol.* **19**, 176–186 (2023). doi: [10.1038/s41589-022-01167-4](https://doi.org/10.1038/s41589-022-01167-4); pmid: [36266353](https://pubmed.ncbi.nlm.nih.gov/36266353/)
57. D. Jia, R. Z. Jurkowska, X. Zhang, A. Jeltsch, X. Cheng, Structure of Dnmt3a bound to Dnmt3L suggests a model for de novo DNA methylation. *Nature* **449**, 248–251 (2007). doi: [10.1038/nature06146](https://doi.org/10.1038/nature06146); pmid: [17713477](https://pubmed.ncbi.nlm.nih.gov/17713477/)
58. N. Veland *et al.*, DNMT3L facilitates DNA methylation partly by maintaining DNMT3A stability in mouse embryonic stem cells. *Nucleic Acids Res.* **47**, 152–167 (2019). doi: [10.1093/nar/gky947](https://doi.org/10.1093/nar/gky947); pmid: [30321403](https://pubmed.ncbi.nlm.nih.gov/30321403/)
59. I. Suetake, F. Shinozaki, J. Miyagawa, H. Takeshima, S. Tajima, DNMT3L stimulates the DNA methylation activity of Dnmt3a and Dnmt3b through a direct interaction. *J. Biol. Chem.* **279**, 27816–27823 (2004). doi: [10.1074/jbc.M400182100](https://doi.org/10.1074/jbc.M400182100); pmid: [15105426](https://pubmed.ncbi.nlm.nih.gov/15105426/)
60. X. Chen, J. L. Zaro, W. C. Shen, Fusion protein linkers: Property, design and functionality. *Adv. Drug Deliv. Rev.* **65**, 1357–1369 (2013). doi: [10.1016/j.addr.2012.09.039](https://doi.org/10.1016/j.addr.2012.09.039); pmid: [23026637](https://pubmed.ncbi.nlm.nih.gov/23026637/)
61. L. W. Koblan *et al.*, Improving cytidine and adenine base editors by expression optimization and ancestral reconstruction. *Nat. Biotechnol.* **36**, 843–846 (2018). doi: [10.1038/nbt.4172](https://doi.org/10.1038/nbt.4172); pmid: [29813047](https://pubmed.ncbi.nlm.nih.gov/29813047/)
62. B. Zeitler, L. Zhang, inventors; Sangamo Therapeutics, assignee. Zinc Finger Protein Transcription Factors for Treatment of Prion Disease. US patent US20230002459A1. (2023).
63. Y. Fang, W. Stroukov, T. Cathomen, C. Mussolino, Chimerization Enables Gene Synthesis and Lentiviral Delivery of Customizable TALE-Based Effectors. *Int. J. Mol. Sci.* **21**, 795 (2020). doi: [10.3390/ijms21030795](https://doi.org/10.3390/ijms21030795); pmid: [31991825](https://pubmed.ncbi.nlm.nih.gov/31991825/)
64. J. M. Levy *et al.*, Cytosine and adenine base editing of the brain, liver, retina, heart and skeletal muscle of mice via adeno-associated viruses. *Nat. Biomed. Eng.* **4**, 97–110 (2020). doi: [10.1038/s41551-019-0501-5](https://doi.org/10.1038/s41551-019-0501-5); pmid: [31937940](https://pubmed.ncbi.nlm.nih.gov/31937940/)
65. A. J. Stevens *et al.*, Design of a Split Intein with Exceptional Protein Splicing Activity. *J. Am. Chem. Soc.* **138**, 2162–2165 (2016). doi: [10.1021/jacs.5b13528](https://doi.org/10.1021/jacs.5b13528); pmid: [26854538](https://pubmed.ncbi.nlm.nih.gov/26854538/)
66. H. S. Li *et al.*, Multidimensional control of therapeutic human cell function with synthetic gene circuits. *Science* **378**, 1227–1234 (2022). doi: [10.1126/science.adf0156](https://doi.org/10.1126/science.adf0156); pmid: [36520914](https://pubmed.ncbi.nlm.nih.gov/36520914/)
67. J. H. Choi *et al.*, Optimization of AAV expression cassettes to improve packaging capacity and transgene expression in neurons. *Mol. Brain* **7**, 17 (2014). doi: [10.1186/1756-6606-7-17](https://doi.org/10.1186/1756-6606-7-17); pmid: [24618276](https://pubmed.ncbi.nlm.nih.gov/24618276/)
68. F. A. Ran *et al.*, In vivo genome editing using *Staphylococcus aureus* Cas9. *Nature* **520**, 186–191 (2015). doi: [10.1038/nature14299](https://doi.org/10.1038/nature14299); pmid: [25830891](https://pubmed.ncbi.nlm.nih.gov/25830891/)
69. K. Y. Chan *et al.*, Engineered AAVs for efficient noninvasive gene delivery to the central and peripheral nervous systems. *Nat. Neurosci.* **20**, 1172–1179 (2017). doi: [10.1038/nn.4593](https://doi.org/10.1038/nn.4593); pmid: [28671695](https://pubmed.ncbi.nlm.nih.gov/28671695/)
70. M. A. Mortberg *et al.*, Regional variability and genotypic and pharmacodynamic effects on PrP concentration in the CNS. *JCI Insight* **7**, e156532 (2022). doi: [10.1172/jci.insight.156532](https://doi.org/10.1172/jci.insight.156532); pmid: [3513987](https://pubmed.ncbi.nlm.nih.gov/3513987/)
71. P. Bankhead *et al.*, QuPath: Open source software for digital pathology image analysis. *Sci. Rep.* **7**, 16878 (2017). doi: [10.1038/s41598-017-2045-4](https://doi.org/10.1038/s41598-017-2045-4); pmid: [29203879](https://pubmed.ncbi.nlm.nih.gov/29203879/)
72. S. Brandner *et al.*, Normal host prion protein necessary for scrapie-induced neurotoxicity. *Nature* **379**, 339–343 (1996). doi: [10.1038/379339a0](https://doi.org/10.1038/379339a0); pmid: [8552188](https://pubmed.ncbi.nlm.nih.gov/8552188/)
73. A. K. K. Lakkaraju *et al.*, Gial activation in prion diseases is selectively triggered by neuronal PrP^{Sc}. *Brain Pathol.* **32**, e13056 (2022). doi: [10.111/bpa.13056](https://doi.org/10.1111/bpa.13056); pmid: [35178783](https://pubmed.ncbi.nlm.nih.gov/35178783/)
74. R. Ibraheim *et al.*, Self-inactivating, all-in-one AAV vectors for precision Cas9 genome editing via homology-directed repair in vivo. *Nat. Commun.* **12**, 6267 (2021). doi: [10.1038/s41467-021-26518-y](https://doi.org/10.1038/s41467-021-26518-y); pmid: [34725353](https://pubmed.ncbi.nlm.nih.gov/34725353/)
75. A. Li *et al.*, A Self-Deleting AAV-CRISPR System for *In Vivo* Genome Editing. *Mol. Ther. Methods Clin. Dev.* **12**, 111–122 (2018). doi: [10.1016/j.omtm.2018.11.009](https://doi.org/10.1016/j.omtm.2018.11.009); pmid: [30619914](https://pubmed.ncbi.nlm.nih.gov/30619914/)
76. M. Subramanian *et al.*, RNAi-mediated rheostat for dynamic control of AAV-delivered transgenes. *Nat. Commun.* **14**, 1970 (2023). doi: [10.1038/s41467-023-37774-5](https://doi.org/10.1038/s41467-023-37774-5); pmid: [37031257](https://pubmed.ncbi.nlm.nih.gov/37031257/)
77. A. Cabrera *et al.*, The sound of silence: Transgene silencing in mammalian cell engineering. *Cell Syst.* **13**, 950–973 (2022). doi: [10.1016/j.cels.2022.11.005](https://doi.org/10.1016/j.cels.2022.11.005); pmid: [36549273](https://pubmed.ncbi.nlm.nih.gov/36549273/)
78. A. S. Khalil *et al.*, A synthetic biology framework for programming eukaryotic transcription functions. *Cell* **150**, 647–658 (2012). doi: [10.1016/j.cell.2012.05.045](https://doi.org/10.1016/j.cell.2012.05.045); pmid: [22863014](https://pubmed.ncbi.nlm.nih.gov/22863014/)
79. C. J. Bashor *et al.*, Complex signal processing in synthetic gene circuits using cooperative regulatory assemblies. *Science* **364**, 593–597 (2019). doi: [10.1126/science.aau8287](https://doi.org/10.1126/science.aau8287); pmid: [31000590](https://pubmed.ncbi.nlm.nih.gov/31000590/)
80. M. D. J. Bragdon *et al.*, Cooperative assembly confers regulatory specificity and long-term genetic circuit stability. *Cell* **186**, 3810–3825.e18 (2023). doi: [10.1016/j.cell.2023.07.012](https://doi.org/10.1016/j.cell.2023.07.012); pmid: [37552983](https://pubmed.ncbi.nlm.nih.gov/37552983/)
81. Y. Ma, M. W. Budde, J. Zhu, M. B. Elowitz, Tuning methylation-dependent silencing dynamics by synthetic modulation of CpG density. *ACS Synth. Biol.* **12**, 2536–2545 (2023). doi: [10.1021/acssynbio.3c00078](https://doi.org/10.1021/acssynbio.3c00078); pmid: [37552041](https://pubmed.ncbi.nlm.nih.gov/37552041/)
82. R. C. Wilson, L. A. Gilbert, The promise and challenge of in vivo delivery for genome therapeutics. *ACS Chem. Biol.* **13**, 376–382 (2018). doi: [10.1021/acschembio.7b00680](https://doi.org/10.1021/acschembio.7b00680); pmid: [29019396](https://pubmed.ncbi.nlm.nih.gov/29019396/)
83. M. Leibowitz *et al.*, Chromothripsy as an on-target consequence of CRISPR-Cas9 genome editing. *Nat. Genet.* **53**, 895–905 (2021). doi: [10.1038/s41588-021-00838-7](https://doi.org/10.1038/s41588-021-00838-7); pmid: [33846636](https://pubmed.ncbi.nlm.nih.gov/33846636/)
84. J. Grünwald *et al.*, Transcriptome-wide off-target RNA editing induced by CRISPR-guided DNA base editors. *Nature* **569**, 433–437 (2019). doi: [10.1038/s41586-019-1161-z](https://doi.org/10.1038/s41586-019-1161-z); pmid: [30995674](https://pubmed.ncbi.nlm.nih.gov/30995674/)
85. E. Zuo *et al.*, Cytosine base editor generates substantial off-target single-nucleotide variants in mouse embryos. *Science* **364**, 289–292 (2019). doi: [10.1126/science.aav9973](https://doi.org/10.1126/science.aav9973); pmid: [30819928](https://pubmed.ncbi.nlm.nih.gov/30819928/)
86. S. Jin *et al.*, Cytosine, but not adenine, base editors induce genome-wide off-target mutations in rice. *Science* **364**, 292–295 (2019). doi: [10.1126/science.aaw7166](https://doi.org/10.1126/science.aaw7166); pmid: [30819931](https://pubmed.ncbi.nlm.nih.gov/30819931/)
87. N. Yan *et al.*, Cytosine base editors induce off-target mutations and adverse phenotypic effects in transgenic mice. *Nat. Commun.* **14**, 1784 (2023). doi: [10.1038/s41467-023-37508-7](https://doi.org/10.1038/s41467-023-37508-7); pmid: [36997536](https://pubmed.ncbi.nlm.nih.gov/36997536/)
88. M. Fiumara *et al.*, Genotoxic effects of base and prime editing in human hematopoietic stem cells. *Nat. Biotechnol.* **2023** (2023). doi: [10.1038/s41587-023-01915-4](https://doi.org/10.1038/s41587-023-01915-4); pmid: [37679541](https://pubmed.ncbi.nlm.nih.gov/37679541/)
89. M. E. Huang *et al.*, C-to-G editing generates double-strand breaks causing deletion, transversion and translocation. *Nat. Cell Biol.* **26**, 294–304 (2024). doi: [10.1038/s41556-023-01342-2](https://doi.org/10.1038/s41556-023-01342-2); pmid: [38263276](https://pubmed.ncbi.nlm.nih.gov/38263276/)
90. G. Hwang *et al.*, Detailed mechanisms for unintended large DNA deletions with CRISPR, base editors, and prime editors. bioRxiv 2024.01.04.574288 [Preprint] (2024). <https://doi.org/10.1101/2024.01.04.574288>.
91. M. G. Kluesner *et al.*, CRISPR-Cas9 cytidine and adenosine base editing of splice-sites mediates highly-efficient disruption of proteins in primary and immortalized cells. *Nat. Commun.* **12**, 1–12 (2021).
92. A. H. Smits *et al.*, Biological plasticity rescues target activity in CRISPR knockouts. *Nat. Methods* **16**, 1087–1093 (2019). doi: [10.1038/s41592-019-0614-5](https://doi.org/10.1038/s41592-019-0614-5); pmid: [31659326](https://pubmed.ncbi.nlm.nih.gov/31659326/)
93. D. A. Kuzmin *et al.*, The clinical landscape for AAV gene therapies. *Nat. Rev. Drug Discov.* **20**, 173–174 (2021). doi: [10.1038/d41573-021-00017-7](https://doi.org/10.1038/d41573-021-00017-7); pmid: [33461515](https://pubmed.ncbi.nlm.nih.gov/33461515/)
94. R. Santos *et al.*, A comprehensive map of molecular drug targets. *Nat. Rev. Drug Discov.* **16**, 19–34 (2017). doi: [10.1038/nrd.2016.230](https://doi.org/10.1038/nrd.2016.230); pmid: [27910877](https://pubmed.ncbi.nlm.nih.gov/27910877/)
95. Q. Ling, J. A. Herstine, A. Bradbury, S. J. Gray, AAV-based in vivo gene therapy for neurological disorders. *Nat. Rev. Drug Discov.* **22**, 789–806 (2023). doi: [10.1038/s41573-023-00766-7](https://doi.org/10.1038/s41573-023-00766-7); pmid: [37658167](https://pubmed.ncbi.nlm.nih.gov/37658167/)
96. S. Zolotukhin, L. H. Vandenberghe, AAV capsid design: A Goldilocks challenge. *Trends Mol. Med.* **28**, 183–193 (2022). doi: [10.1016/j.molmed.2022.01.003](https://doi.org/10.1016/j.molmed.2022.01.003); pmid: [35093287](https://pubmed.ncbi.nlm.nih.gov/35093287/)
97. Q. Huang *et al.*, An AAV capsid reprogrammed to bind human Transferrin Receptor mediates brain-wide gene delivery. *Science* **384**, 1220–1227 (2024). doi: [10.1126/science.adm8386](https://doi.org/10.1126/science.adm8386)
98. J. Khirallah, M. Einbinder, Y. Li, Q. Xu, Clinical progress in genome-editing technology and in vivo delivery techniques.

- Trends Genet.* **39**, 208–216 (2023). doi: [10.1016/j.tig.2022.12.001](https://doi.org/10.1016/j.tig.2022.12.001); pmid: [36669950](https://pubmed.ncbi.nlm.nih.gov/36669950/)
99. S. Banskota *et al.*, Engineered virus-like particles for efficient in vivo delivery of therapeutic proteins. *Cell* **185**, 250–265.e16 (2022). doi: [10.1016/j.cell.2021.12.021](https://doi.org/10.1016/j.cell.2021.12.021); pmid: [35021064](https://pubmed.ncbi.nlm.nih.gov/35021064/)
100. E. V. Minikel *et al.*, Prion protein lowering is a disease-modifying therapy across prion disease stages, strains and endpoints. *Nucleic Acids Res.* **48**, 10615–10631 (2020). doi: [10.1093/nar/gkaa616](https://doi.org/10.1093/nar/gkaa616); pmid: [32776089](https://pubmed.ncbi.nlm.nih.gov/32776089/)
101. J. P. Zhang *et al.*, Efficient precise knockin with a double cut HDR donor after CRISPR/Cas9-mediated double-stranded DNA cleavage. *Genome Biol.* **18**, 35 (2017). doi: [10.1186/s13059-017-1164-8](https://doi.org/10.1186/s13059-017-1164-8); pmid: [28219395](https://pubmed.ncbi.nlm.nih.gov/28219395/)
102. J. G. Doench *et al.*, Optimized sgRNA design to maximize activity and minimize off-target effects of CRISPR-Cas9. *Nat. Biotechnol.* **34**, 184–191 (2016). doi: [10.1038/nbt.3437](https://doi.org/10.1038/nbt.3437); pmid: [26780180](https://pubmed.ncbi.nlm.nih.gov/26780180/)
103. S. F. Altschul, W. Gish, W. Miller, E. W. Myers, D. J. Lipman, Basic local alignment search tool. *J. Mol. Biol.* **215**, 403–410 (1990). doi: [10.1016/S0022-2836\(05\)80360-2](https://doi.org/10.1016/S0022-2836(05)80360-2); pmid: [2231712](https://pubmed.ncbi.nlm.nih.gov/2231712/)
104. K. Katoh, D. M. Standley, MAFFT multiple sequence alignment software version 7: Improvements in performance and usability. *Mol. Biol. Evol.* **30**, 772–780 (2013). doi: [10.1093/molbev/mst010](https://doi.org/10.1093/molbev/mst010); pmid: [2329690](https://pubmed.ncbi.nlm.nih.gov/2329690/)
105. L. T. Nguyen, H. A. Schmidt, A. von Haeseler, B. Q. Minh, IQ-TREE: A fast and effective stochastic algorithm for estimating maximum-likelihood phylogenies. *Mol. Biol. Evol.* **32**, 268–274 (2015). doi: [10.1093/molbev/msu300](https://doi.org/10.1093/molbev/msu300); pmid: [25371430](https://pubmed.ncbi.nlm.nih.gov/25371430/)
106. I. Letunic, P. Bork, Interactive Tree Of Life (iTOL) v5: An online tool for phylogenetic tree display and annotation. *Nucleic Acids Res.* **49**, W293–W296 (2021). doi: [10.1093/nar/gkab301](https://doi.org/10.1093/nar/gkab301); pmid: [33885785](https://pubmed.ncbi.nlm.nih.gov/33885785/)
107. E. Neumann, CHARM, a Prion, Version v1, Zenodo (2024); <https://doi.org/10.5281/zenodo.11099261>.
108. Y. Zhang *et al.*, Deciphering TAL effectors for 5-methylcytosine and 5-hydroxymethylcytosine recognition. *Nat. Commun.* **8**, 901 (2017). doi: [10.1038/s41467-017-00860-6](https://doi.org/10.1038/s41467-017-00860-6); pmid: [29026078](https://pubmed.ncbi.nlm.nih.gov/29026078/)
109. J. C. Miller *et al.*, Improved specificity of TALE-based genome editing using an expanded RVD repertoire. *Nat. Methods* **12**, 465–471 (2015). doi: [10.1038/nmeth.3330](https://doi.org/10.1038/nmeth.3330); pmid: [25799440](https://pubmed.ncbi.nlm.nih.gov/25799440/)
110. K. Labun *et al.*, CHOPCHOP v3: Expanding the CRISPR web toolbox beyond genome editing. *Nucleic Acids Res.* **47**, W171–W174 (2019). doi: [10.1093/nar/gkz365](https://doi.org/10.1093/nar/gkz365); pmid: [31106371](https://pubmed.ncbi.nlm.nih.gov/31106371/)
111. J. T. Robinson *et al.*, Integrative genomics viewer. *Nat. Biotechnol.* **29**, 24–26 (2011). doi: [10.1038/nbt.1754](https://doi.org/10.1038/nbt.1754); pmid: [21221095](https://pubmed.ncbi.nlm.nih.gov/21221095/)
112. Y. Liao, G. K. Smyth, W. Shi, featureCounts: An efficient general purpose program for assigning sequence reads to genomic features. *Bioinformatics* **30**, 923–930 (2014). doi: [10.1093/bioinformatics/btt656](https://doi.org/10.1093/bioinformatics/btt656); pmid: [24227677](https://pubmed.ncbi.nlm.nih.gov/24227677/)
113. M. I. Love, W. Huber, S. Anders, Moderated estimation of fold change and dispersion for RNA-seq data with DESeq2. *Genome Biol.* **15**, 550 (2014). doi: [10.1186/s13059-014-0550-8](https://doi.org/10.1186/s13059-014-0550-8); pmid: [25516281](https://pubmed.ncbi.nlm.nih.gov/25516281/)
114. Y. Kumaki, M. Oda, M. Okano, QUMA: Quantification tool for methylation analysis. *Nucleic Acids Res.* **36**, W170–W175 (2008). doi: [10.1093/nar/gkn294](https://doi.org/10.1093/nar/gkn294); pmid: [18487274](https://pubmed.ncbi.nlm.nih.gov/18487274/)
115. J. R. Davis *et al.*, Efficient in vivo base editing via single adeno-associated viruses with size-optimized genomes encoding compact adenine base editors. *Nat. Biomed. Eng.* **6**, 1272–1283 (2022). doi: [10.1038/s41551-022-00911-4](https://doi.org/10.1038/s41551-022-00911-4); pmid: [35902773](https://pubmed.ncbi.nlm.nih.gov/35902773/)
116. A. G. Reidenbach *et al.*, Multimodal small-molecule screening for human prion protein binders. *J. Biol. Chem.* **295**, 13516–13531 (2020). doi: [10.1074/jbc.RA120.014905](https://doi.org/10.1074/jbc.RA120.014905); pmid: [32723867](https://pubmed.ncbi.nlm.nih.gov/32723867/)
117. H. M. T. Choi *et al.*, Third-generation *in situ* hybridization chain reaction: Multiplexed, quantitative, sensitive, versatile, robust. *Development* **145**, dev165753 (2018). doi: [10.1242/dev.165753](https://doi.org/10.1242/dev.165753); pmid: [29945988](https://pubmed.ncbi.nlm.nih.gov/29945988/)
118. J. Schindelin *et al.*, Fiji: An open-source platform for biological-image analysis. *Nat. Methods* **9**, 676–682 (2012). doi: [10.1038/nmeth.2019](https://doi.org/10.1038/nmeth.2019); pmid: [22743772](https://pubmed.ncbi.nlm.nih.gov/22743772/)
119. M. A. Cappelluti *et al.*, Durable and efficient gene silencing in vivo by hit-and-run epigenome editing. *Nature* **627**, 416–423 (2024). doi: [10.1038/s41586-024-07087-8](https://doi.org/10.1038/s41586-024-07087-8); pmid: [38418872](https://pubmed.ncbi.nlm.nih.gov/38418872/)
- ACKNOWLEDGMENTS**
We thank W. Allen, K. Chan, Y. Chen, K. Joung, G. Muthukumar, A. Refermat, J. Sandhu, F. Urnov, A. White, K. Yost, P. Zheng, the CellProfiler team at the Broad Institute, and members of the Weissman, Lababidi/Minikel, and Liu labs for useful advice and discussion. We are grateful to A. Marcos Vidal and C. Rogers from the Keck Imaging Facility at the Whitehead Institute; S. Mraz, J. Lover, and S. Gupta from the Genome Technology Core at the Whitehead Institute; K. Cormier and C. Codon at the Hope Babette Tang Histology Facility in the Koch Institute's Robert A. Swanson Biotechnology Center; and J. Yusuf for technical assistance. Figures were created with elements from BioRender.com. **Funding:** This work was supported by the National Institutes of Health (NIH) Common Fund Program, Somatic Cell Genome Editing, through an award administered by the National Institute of Neurodegenerative Disorders and Stroke (NINDS) (5U19NS132315) to PIs S.M.V., E.V.M., J.S.W., and B.E.D.; NIH grants 2RM1HG009490-07 (to J.S.W.) and R01EB029483 (to A.S.K.); the Jane Coffin Childs Memorial Fund (to T.M.B.); the Department of Defense Vannevar Bush Faculty Fellowship (N00014-20-1-2825 to A.S.K.); and the Schmidt Science Polymath Award (G-22-63292 to A.S.K.). J.S.W. is an HHMI investigator. **Author contributions:** J.S.W., S.M.V., E.V.M., E.N.N., T.M.B., and B.E.D. designed and interpreted the research. E.N.N. conceived of CHARM and led its development with help from E.W. and T.M.B. T.M.B. led the development of self-silencing strategies with help from E.W., E.N.N., M.H.R., and A.S.K. AAVs were produced and characterized by J.W.H., P.P.B., and C.P.P. F.S. and A.C. oversaw and conducted animal studies with help from M.H., K.L., and K.G. T.M.B., E.N.N., E.W., F.S., and N.K. characterized animal studies. J.S.W., S.M.V., E.V.M., and B.E.D. acquired funding and supervised the project. E.N.N., T.M.B., and J.S.W. wrote the manuscript with input from all authors. **Competing interests:** J.S.W. declares outside interest in 5 AM Venture, Amgen, Chroma Medicine, KSQ Therapeutics, Maze Therapeutics, Tenaya Therapeutics, Tessa Therapeutics, Ziada Therapeutics, and Third Rock Ventures. S.M.V. acknowledges speaking fees from Ultragenyx, Illumina, Biogen, and Eli Lilly; consulting fees from Invitae and Alnylam; and research support from Ionis, the Bill and Melinda Gates Foundation, and Sangamo Therapeutics. E.V.M. acknowledges speaking fees from Eli Lilly; consulting fees from Deerfield and Alnylam; and research support from Ionis, the Bill and Melinda Gates Foundation, Sangamo Therapeutics, and Eli Lilly. A.S.K. is a scientific adviser for and holds equity in Senti Biosciences and Chroma Medicine and is a cofounder of Fynch Biosciences and K2 Biotechnologies. E.N.N., T.M.B., and J.S.W. are co-inventors on US patent application 18/444,590 filed by the Whitehead Institute, relating to CHARM and self-silencing AAVs. E.N.N., T.M.B., J.S.W., E.V.M., and S.M.V. are co-inventors on provisional US patent application 63/623,787 filed jointly by the Whitehead Institute and Broad Institute relating to ZFcharms for prion disease. B.E.D. declares outside interest in Apertura Gene Therapy and Tevard Biosciences and is an inventor on US patent application US1499165B2 relating to the PHP.eB AAV capsid. All other authors declare that they have no competing interests. **Data and materials availability:** RNA-seq datasets are available at the Gene Expression Omnibus (GEO) (GSE255987). Expression plasmids are available from Addgene under a uniform biological material transfer agreement. All other data are available in the manuscript or the supplementary materials. Custom scripts for genome mining and nanopore sequencing analysis are available at Zenodo ([10.5281/zenodo.11099261](https://doi.org/10.5281/zenodo.11099261)). **License information:** Copyright © 2024 the authors, some rights reserved; exclusive licensee American Association for the Advancement of Science. No claim to original US government works. <https://www.science.org/about/science-licenses-journal-article-reuse> This article is subject to HHMI's Open Access to Publications policy. HHMI lab heads have previously granted a nonexclusive CC BY 4.0 license to the public and a sublicensable license to HHMI in their research articles. Pursuant to those licenses, the author-accepted manuscript (AAM) of this article can be made freely available under a CC BY 4.0 license immediately upon publication.
- SUPPLEMENTARY MATERIALS**
science.org/doi/10.1126/science.ad07082
Figs. S1 to S13
Tables S1 and S2
MDAR Reproducibility Checklist
- Submitted 18 February 2024; accepted 2 May 2024
10.1126/science.ad07082